

Suppression of mesoscale eddy mixing by topographic PV gradients

Miriam F. Sterl,^{a,b} Joseph H. LaCasce,^c Sjoerd Groeskamp,^a Aleksi Nummelin,^{d,e} Pål E. Isachsen,^{c,f} Michiel L. J. Baatsen^b

^a *NIOZ Royal Netherlands Institute for Sea Research, Texel, The Netherlands*

^b *Institute for Marine and Atmospheric Research, Utrecht University, Utrecht, The Netherlands*

^c *Department of Geosciences, University of Oslo, Oslo, Norway*

^d *NORCE Norwegian Research Centre AS, Bergen, Norway*

^e *Finnish Meteorological Institute, Helsinki, Finland*

^f *Norwegian Meteorological Institute, Oslo, Norway*

Corresponding author: Miriam F. Sterl, miriam.sterl@nioz.nl

11 ABSTRACT: Oceanic mesoscale eddy mixing plays a crucial role in the Earth’s climate system
12 by redistributing heat, salt and carbon. For many ocean and climate models, mesoscale eddies
13 still need to be parameterized. This is often done via an eddy diffusivity, \mathcal{K} , which sets the
14 strength of turbulent downgradient tracer fluxes. A well known effect is the modulation of \mathcal{K} in
15 the presence of background potential vorticity (PV) gradients, which suppresses cross-PV gradient
16 mixing. Topographic slopes can induce such suppression through topographic PV gradients.
17 However, this effect has received little attention, and topographic effects are often not included
18 in parameterizations for \mathcal{K} . In this study, we show that it is possible to describe the effect of
19 topography on \mathcal{K} analytically in a barotropic framework, using a simple stochastic representation
20 of eddy-eddy interactions. We obtain an analytical expression for the depth-averaged \mathcal{K} as a
21 function of the bottom slope, which we validate against diagnosed eddy diffusivities from a
22 numerical model. The obtained analytical expression can be generalized to any constant barotropic
23 PV gradient. Moreover, the expression is consistent with empirical parameterizations for eddy
24 diffusivity over topography from previous studies and provides a physical rationalization for these
25 parameterizations. The new expression helps to understand how eddy diffusivities vary across the
26 ocean, and thus how mesoscale eddies impact ocean mixing processes.

27 SIGNIFICANCE STATEMENT: Large oceanic ‘whirls’, called eddies, can mix and transport
28 ocean properties such as heat, salt, carbon and nutrients. Mixing plays an important role for
29 oceanic ecosystems and the climate system. In numerical simulations of the Earth’s climate, eddy
30 mixing is typically represented using a simplified expression. However, an effect that is often not
31 included is that eddy mixing is weaker over a sloping seafloor. In most areas of the ocean the
32 bottom slope is steep enough for this effect to be significant. In this study we derive an expression
33 for eddy mixing that accounts for oceanic bottom slopes. The present effort provides a physical
34 basis for eddy mixing over oceanic bottom slopes, justifying their use in climate models.

35 1. Introduction

36 Oceanic mesoscale eddies play a key role in the global ocean circulation, oceanic ecosystems and
37 the climate system as a whole. Eddies mix, transport, and store tracers such as heat, salt, carbon,
38 oxygen, and nutrients (Lee et al. 2007; Gruber et al. 2011; Gnanadesikan et al. 2013, 2015, 2017;
39 Stewart et al. 2018; Busecke and Abernathey 2019; Jones and Abernathey 2019; Groeskamp et al.
40 2019). However, mesoscale eddies occur on spatial scales of 10–100 km, which is in the same
41 order or smaller than the horizontal grid resolution of most global climate models (Eden 2007;
42 Chelton et al. 2011; Hallberg 2013; LaCasce and Groeskamp 2020; Martínez-Moreno et al. 2022).
43 Therefore, mesoscale mixing processes are often not explicitly resolved in climate simulations,
44 and instead need to be parameterized (Eden and Greatbatch 2008; Hallberg 2013; Jansen et al.
45 2015; Zanna et al. 2017; Fox-Kemper et al. 2019; Wang and Stewart 2020). Parameterization of
46 eddy mixing is typically done via an eddy diffusivity, \mathcal{K} , which relates the turbulent downgradient
47 flux of a tracer \mathcal{F}_C to the mean lateral tracer gradient ∇C as $\mathcal{F}_C = -\mathcal{K}\nabla C$. A distinction can be
48 made between buoyancy diffusivity, which describes an eddy induced advection that resembles a
49 diffusion of buoyancy (Gent and McWilliams 1990; Gent et al. 1995; McDougall and McIntosh
50 2001), and isopycnal diffusivity representing eddy diffusive fluxes that mix tracers along isopycnals
51 (Redi 1982; Griffies 1998).

52 Significantly, climate models are very sensitive to the choice of the diffusivity value (e.g. Ferreira
53 et al. 2005; Pradal and Gnanadesikan 2014; Gnanadesikan et al. 2015; Kjellsson and Zanna 2017;
54 Jones and Abernathey 2019; Holmes et al. 2022; Mak et al. 2022b). In simulations of the Earth’s
55 climate, an approximately five-fold increase in the value of \mathcal{K} can result in differences of 1°C in

56 the global-mean surface air and sea surface temperatures (Pradal and Gnanadesikan 2014), 20%
57 variation in anthropogenic carbon uptake (Gnanadesikan et al. 2015), and a decrease in the residual
58 meridional overturning circulation in the North Atlantic and the Antarctic Circumpolar Current
59 volume transport in the Southern Ocean by around 30% (Chouksey et al. 2022). It is thus of great
60 importance to know how to accurately parameterize \mathcal{K} in global climate models.

61 Many parameterizations of \mathcal{K} are based on mixing length theory (Prandtl 1925), which suggests
62 a scaling of the form $K \sim \mathcal{V}\mathcal{L}$, where \mathcal{V} is the root mean squared eddy velocity and \mathcal{L} is a mixing
63 length. The mixing length can be thought of as a length scale over which the eddy field can
64 effectively mix tracers. Mixing length theory was applied to create the first global estimates of
65 eddy diffusivity at the sea surface (Holloway 1986; Keffer and Holloway 1988; Stammer 1998).

66 Holloway and Kristmannsson (1984) and Holloway (1986) suggested that if eddies have Rossby
67 wave characteristics, the eddy diffusivity is suppressed. This suppression effect was later shown
68 analytically by e.g. Ferrari and Nikurashin (2010) (using a passive tracer approach), Klocker et al.
69 (2012) (using a Lagrangian approach), and Griesel et al. (2015) (using linear stability analysis). In
70 all of these studies, eddy fields are represented as statistically forced and linearly damped Rossby
71 waves, and it is shown that the cross-stream mixing length is effectively reduced in the presence of
72 a background mean flow if the eddies are propagating relative to the mean flow.

73 A kinematic interpretation of the suppression mechanism is that the mean flow will advect
74 tracers through the eddy field before the eddy field has had time to mix the tracers in the cross-
75 stream direction. If the eddies did not have an intrinsic phase speed, they would move with the
76 mean flow and thus be able to effectively mix the tracers. The parameterization of Ferrari and
77 Nikurashin (2010) has been widely used in idealized models (Nakamura and Zhu 2010b; Eden
78 2011; Srinivasan and Young 2014; Kong and Jansen 2017; Wolfram and Ringler 2017; Seland
79 et al. 2020) and validated and applied to the Antarctic Circumpolar Current (Naveira Garabato
80 et al. 2011; Sallée et al. 2011; Meredith et al. 2012; Pennel and Kamenkovich 2014; Chen et al.
81 2015; Roach et al. 2016; Chapman and Sallée 2017), the Kuroshio Extension (Chen et al. 2014),
82 the Gulf Stream (Bolton et al. 2019), the Nordic Seas (Isachsen and Nøst 2012), eastern boundary
83 currents (Bire and Wolfe 2018), and the global ocean (Bates et al. 2014; Klocker and Abernathey
84 2014; Roach et al. 2018; Busecke and Abernathey 2019; Canuto et al. 2019; Groeskamp et al.
85 2020).

86 A different interpretation from the kinematic explanation described above is that the suppression
87 is a dynamical effect caused by gradients in potential vorticity (PV). Marshall et al. (2006) estimated
88 surface eddy diffusivities in the Southern Ocean from satellite altimetry, and found that regions of
89 high and low diffusivity coincide with regions of weak and strong PV gradients, respectively. They
90 suggested that strong PV gradients impose a barrier on lateral transport, inhibiting cross-stream
91 diffusivity. This effect is also observed in the atmosphere (e.g. Dritschel and McIntyre 2008).
92 Nakamura and Zhu (2010b), Klocker et al. (2012), Srinivasan and Young (2014) and Balwada
93 et al. (2016) explicitly linked the mixing barriers caused by PV gradients to the parameterization
94 of Ferrari and Nikurashin (2010) by noting that the PV gradient determines the Rossby wave phase
95 speed; hence, it is the PV gradient that enables the eddies to move relative to the mean flow, which
96 leads to the suppression of the cross-stream eddy diffusivity.

97 Previous studies have mainly focused on PV gradients caused by the planetary β -effect (latitudinal
98 variations of the Coriolis parameter). However, an important factor that should also be considered
99 is the effect of topography. If it is indeed the PV gradient that causes the suppression effect, then we
100 must consider the role of topography as well, because topographic slopes contribute significantly
101 to (barotropic) PV gradients (LaCasce and Speer 1999; LaCasce 2000) and permit topographic
102 Rossby waves (Rhines 1970; Csanady 1976; Hogg 2000). Hence, topographic slopes can also
103 be expected to modulate eddy diffusivity (Jansen et al. 2015). Isachsen (2011) diagnosed eddy
104 diffusivities for different bottom slopes from numerical simulations, and found that the diffusivities
105 were highest for flat bottoms, suggesting a suppression effect of topographic slopes. A relevant
106 question then is how exactly does topography modulate eddy diffusivities, and how to parameterize
107 topographic effects related to eddy mixing. Since topography steers currents, its effects might
108 already be included in the mean flow term from Ferrari and Nikurashin (2010), but only implicitly.

109 Some recent studies have aimed to express the eddy diffusivity explicitly in terms of topographic
110 slopes using numerical model data. Diagnostic expressions were derived from high-resolution
111 simulations by Brink (2012), Brink and Cherian (2013) and Brink (2016), by Wang and Stewart
112 (2020) and Wei et al. (2022) for buoyancy diffusivity specifically, and by Wei and Wang (2021)
113 for isopycnal diffusivity specifically. Moreover, Nummelin and Isachsen (2024) and Wei et al.
114 (2024) derived parameterizations for the buoyancy diffusivity over topographic slopes and tested
115 them in prognostic coarse-resolution simulations. All of these studies derived parameterizations

for the eddy diffusivities using various scaling estimates for the mixing length combined with empirical ‘suppression’ functions. Although the suppression functions from the aforementioned studies perform well in representing suppression of eddy diffusivity by topographic slopes, they are essentially empirical fits to functions that have little dynamical justification. Therefore, the aim of this study is to derive an analytical expression for the suppression of \mathcal{K} that is dynamically linked to the topographic PV gradient. Such an expression can provide insight into the physical mechanisms through which topography suppresses eddy diffusivities. On a practical level, it can also help in making more accurate estimates of eddy diffusivities across the world’s oceans. The focus of this work is on the suppression effect of topography, without particularly focusing on buoyancy or isopycnal diffusivity. Diagnosing diffusivity will be done with downgradient fluxes of both buoyancy and PV.

The rest of this article is organized as follows. In section 2, we derive the analytical model. In section 3, we compare the analytical expression for \mathcal{K} with diagnosed diffusivities from a numerical model. Section 4 discusses the theoretical and numerical results. Finally, a summary and conclusion are given in section 5.

2. Theory

The starting point is the Quasi-Geostrophic Potential Vorticity (QGPV) equation. As we are interested in the effects of topographic PV, we work with the barotropic QGPV equation, which explicitly includes a topographic PV term. The barotropic and rigid lid QGPV equation on a β -plane, in the absence of forcing and dissipation, says that the QGPV, q [s^{-1}], is materially conserved (e.g. Dijkstra 2008):

$$\frac{d_g}{dt}q = 0, \quad q = \underbrace{\nabla^2\psi}_{\text{relative vorticity}} + \underbrace{\beta_0 y}_{\text{planetary PV}} + \underbrace{\frac{f_0}{H}h_b}_{\text{topographic PV}}. \quad (1)$$

Here $\frac{d_g}{dt} = \partial_t + u_g \partial_x + v_g \partial_y$, where u_g and v_g [m s^{-1}] are the zonal and meridional geostrophic velocities, which are related to the geostrophic streamfunction ψ [$\text{m}^2 \text{s}^{-1}$] as $(u_g, v_g) = (-\partial\psi/\partial y, \partial\psi/\partial x)$. Furthermore, f_0 [s^{-1}] is the Coriolis parameter at some fixed latitude φ_0 and β_0 [$\text{m}^{-1} \text{s}^{-1}$] is the meridional gradient of the Coriolis parameter at φ_0 ; both f_0 and β_0 are assumed constant here

141 (β -plane approximation). The meridional coordinate relative to φ_0 is denoted by y [m]. Finally,
 142 H [m] is the mean water depth, while $h_b = h_b(x, y)$ [m] is the topographic variation superimposed
 143 on H , with $|h_b| \ll H$.

144 We decompose ψ , q and \mathbf{u}_g into time-mean components (denoted by Ψ, Q, \mathbf{U}) and eddy com-
 145 ponents (denoted by ψ', q', \mathbf{u}'). The velocities and streamfunctions are related to each other as
 146 $\mathbf{U} = (-\partial\Psi/\partial y, \partial\Psi/\partial x)$ and $\mathbf{u}' = (-\partial\psi'/\partial y, \partial\psi'/\partial x)$. We assume that the mean flow varies on
 147 spatial scales much larger than the eddy field; hence, it is approximately constant in both space and
 148 time. Then the mean relative vorticity $\nabla^2\Psi = 0$, so that the mean PV is determined by the planetary
 149 PV and topographic PV. Additionally, we assume that the mean flow \mathbf{U} is parallel to mean PV con-
 150 tours (Pedlosky 1987; Vallis and Maltrud 1993), so that $\mathbf{U} \cdot \nabla Q = 0$. We then rotate the coordinate
 151 system such that the x -direction is aligned with the direction of the mean PV contours. Hence, the
 152 mean flow can be expressed as $\mathbf{U} = (U, 0)$; furthermore, the mean PV gradient is $\nabla Q = (0, \partial Q/\partial y)$,
 153 which we assume to be constant. With these assumptions the QGPV equation can be rewritten as

$$\frac{\partial q'}{\partial t} + \mathbf{U} \cdot \nabla q' + \mathbf{u}' \cdot \nabla Q = \mathcal{N}, \quad (2)$$

154 where \mathcal{N} denotes the nonlinear terms $\mathbf{u}' \cdot \nabla q'$, interpreted as eddy-eddy interactions. Note that
 155 equation (2) is Galilean invariant.

156 From here, the derivation is analogous to that of Klocker et al. (2012), and we only discuss
 157 the key steps below; details of the derivation can be found in Appendix A. We express the eddy
 158 streamfunction ψ' as a monochromatic Rossby wave, given by

$$\psi'(x, y, t) = \text{Re} \left(a(t) e^{ikx + il y} \right), \quad (3)$$

159 where k and l are the zonal and meridional wavenumbers, respectively. Substituting (3) into (2)
 160 and using (1) to relate q' to ψ' , we obtain an ordinary differential equation for the wave amplitude
 161 $a(t)$, given by:

$$\frac{da}{dt} + ik c_w a = \mathcal{N}. \quad (4)$$

Here c_w is the total eddy phase speed relative to the ground (or eddy drift speed), which can be written as:

$$c_w = U + c, \quad c = -\frac{\partial Q / \partial y}{\kappa^2}, \quad (5)$$

where $\kappa \equiv \sqrt{k^2 + l^2}$ is the wavenumber magnitude and c is the intrinsic Rossby wave phase speed relative to the mean flow, given by the dispersion relation for Rossby waves (e.g. Dijkstra 2008). To obtain analytical solutions to (4), we assume the nonlinear eddy-eddy interactions have a fluctuation-dissipation stochastic representation (DelSole 2004; Ferrari and Nikurashin 2010; Klocker et al. 2012), given by

$$\mathcal{N} = Ar(t) - \gamma a(t). \quad (6)$$

Here, $r(t)$ is a white noise random process with A setting its amplitude. Energy dissipates through linear damping, and γ is the damping rate or inverse eddy decorrelation timescale. It is called a ‘decorrelation’ timescale because the cross-stream eddy velocity autocovariance decays exponentially in time with γ^{-1} the e -folding timescale (equation A14 in Appendix A). Combining (4) and (6) and expressing the eddy kinetic energy (EKE), $\mathcal{U}^2/2$, in terms of the eddy velocities as

$$\mathcal{U}^2 = \langle u'^2 \rangle + \langle v'^2 \rangle, \quad (7)$$

it is possible to find an analytical solution for $a(t)$ (see equations A1–A7 in Appendix A). Given $a(t)$, we can get an expression for the eddy streamfunction $\psi'(x, y, t)$ (equation A8), which then gives us expressions for the eddy flow velocities. From knowledge of the eddy flow velocities, we can then compute eddy diffusivities. We will focus on the diffusivity in the cross-stream direction (here: y) because in the along-stream direction advection by the mean flow is dominant over eddy diffusion (LaCasce et al. 2014). We compute the eddy diffusivity as the Taylor diffusivity (Taylor 1921), which applies to passive tracer particles and is defined as the derivative of the mean squared separation of particles from their starting position. The Taylor diffusivity can also be written as the autocorrelation of the Lagrangian cross-stream eddy velocity (Taylor 1921; Davis 1987, 1991;

LaCasce 2008; LaCasce et al. 2014):

$$\mathcal{K} = \lim_{t \rightarrow \infty} \frac{1}{2} \frac{d}{dt} \eta^2 = \lim_{t \rightarrow \infty} \text{Re} \left(\int_0^t \langle v_L(t) v_L^*(t') \rangle dt' \right), \quad (8)$$

where η is the particle displacement and $v_L = v_L(t; x, y, 0)$ is the Lagrangian velocity of a particle at time t that was at (x, y) at $t = 0$. We approximate $v_L(t; x, y, 0)$ with the Eulerian velocity for a particle advected by the mean flow, $v'(x + Ut, y, t)$, for which we can get an analytical expression via the streamfunction relation $v' = -\partial\psi'/\partial x$. This finally gives us the following expression for the cross-stream eddy diffusivity (see equations A9–A17 in Appendix A):

$$\mathcal{K} = \frac{\mathcal{K}_0}{1 + \frac{k^2}{\gamma^2} (c_w - U)^2} \equiv \mathcal{S} \mathcal{K}_0, \quad (9)$$

with

$$\mathcal{K}_0 \equiv \frac{\mathcal{A} \mathcal{U}^2}{\gamma}. \quad (10)$$

Here, $\mathcal{A} = k^2/\kappa^2$ is the eddy anisotropy factor (Wei and Wang 2021), representing the magnitude of the along-stream wavenumber relative to the total wavenumber magnitude. The factor \mathcal{S} is the ‘suppression factor’, and \mathcal{K}_0 is the unsuppressed diffusivity. Note that \mathcal{K}_0 follows a mixing length scaling (Prandtl 1925) where the mixing length is set by $\mathcal{L} = \mathcal{U}/\gamma$, i.e. the mixing length depends on the EKE. As noted by Ferrari and Nikurashin (2010), from (9) it can be seen that the eddy diffusivity is suppressed if $c_w - U \neq 0$, i.e. if the eddies have an intrinsic phase speed and are moving relative to the mean flow. Suppression is strong when $k(c_w - U) \gg \gamma$, i.e. when the advection timescale is shorter than the eddy decorrelation timescale. On the other hand, if the eddy field decorrelates faster than the advective timescale, i.e. $k(c_w - U) \ll \gamma$, the suppression effect is negligible. Equation (9) is equivalent to equation (14) of Ferrari and Nikurashin (2010) and equation (20) of Klocker et al. (2012), and has been applied in many studies. Note that (9) is a general expression that applies to any form of the barotropic QGPV equation (1) assuming a constant PV gradient.

One can also express \mathcal{K} in terms of the PV gradient by using equation (5) to replace the mean flow term $c_w - U$ in (9) by c , the intrinsic eddy phase speed. The intrinsic phase speed is determined by

the PV gradient via the dispersion relation for Rossby waves:

$$|c| = \frac{|\nabla Q|}{\kappa^2}. \quad (11)$$

Substituting (11) and the expression for the anisotropy factor, $\mathcal{A} = k^2/\kappa^2$, into (9) gives the following:

$$\mathcal{K} = \frac{\mathcal{K}_0}{1 + \frac{\mathcal{A}}{\gamma^2 \kappa^2} |\nabla Q|^2}. \quad (12)$$

Equation (12) demonstrates that the eddy diffusivity is suppressed not by the mean flow per se but by the presence of background PV gradients. The diffusivity is inversely proportional to the squared PV gradient (see also Nakamura and Zhu 2010b); the stronger the PV gradient, the stronger the suppression.

Equations (9) and (12) both describe suppression of eddy mixing, but offering different interpretations. Equation (9) expresses suppression in terms of the mean flow and the eddy phase speed, while (12) expresses the suppression in terms of the PV gradient directly. The ‘velocity formulation’ (9) has been used frequently before (Ferrari and Nikurashin 2010; Klocker et al. 2012), while the ‘PV formulation’ (12) was noted by Nakamura and Zhu (2010a) and Klocker et al. (2012). We use the PV form, recognizing that the mean velocity should drop out of the problem, due to the Galilean invariance noted earlier.

For simplicity, we focus on the f -plane case with a linear topographic PV gradient. Including the β -effect does not change the results qualitatively but merely requires rotating the coordinate system. The PV contours are thus parallel to the isobaths and $|\nabla Q| = \frac{f_0}{H} |\nabla h_b| \equiv \frac{f_0}{H} \alpha$. This yields an expression of the cross-slope diffusivity in terms of the topographic slope, α :

$$\mathcal{K} = \frac{\mathcal{K}_0}{1 + \frac{f_0^2 \mathcal{A}}{\gamma^2 \kappa^2 H^2} \alpha^2}. \quad (13)$$

Note \mathcal{K} is independent of the slope direction.

To evaluate the expression for \mathcal{K} , we require the wavenumber κ . We assume κ is given by $1/L$, where L is the dominant length scale of the eddies. We consider two options: the internal or first baroclinic Rossby radius, L_{Rossby} , and the topographic Rhines scale, L_{Rhines} . The first baroclinic

227 Rossby radius is given by:

$$L_{\text{Rossby}} \propto \frac{NH}{|f_0|}, \quad (14)$$

228 where N is the depth-averaged buoyancy frequency (e.g. Chelton et al. 1998). This is the ap-
 229 proximate scale of the fastest growing mode in the Eady model for baroclinic instability (Eady
 230 1949). Even though internal PV gradients (planetary β or layer thickness gradients) can introduce
 231 other scales (Charney 1947; Green 1960), L_{Rossby} remains a much used estimate of the eddy length
 232 scale (e.g. Hallberg 2013; LaCasce and Groeskamp 2020; Groeskamp et al. 2020). Of course the
 233 Rossby radius is relevant for a stratified flow whereas our derivation is based on the barotropic
 234 QGPV equation. The rationale is that the process setting the dominant wavelength is conversion of
 235 energy from the baroclinic to the barotropic mode, with the active dynamics then being barotropic
 236 (Larichev and Held 1995; Yankovsky et al. 2022).

237 Second, the topographic Rhines scale is given by:

$$L_{\text{Rhines}} \propto \sqrt{\frac{\mathcal{U}}{|\nabla Q|}} = \sqrt{\frac{\mathcal{U}}{f_0|\alpha|/H}}. \quad (15)$$

238 The topographic Rhines scale represents the maximum length scale in an inverse cascade and the
 239 transition between turbulence and topographic waves (e.g. Brink 2017). The ‘standard’ Rhines
 240 scale, which considers planetary Rossby waves instead of topographic waves and is equal to
 241 $\sqrt{\mathcal{U}/\beta}$ (Vallis and Maltrud 1993), is found to be a good estimate of the eddy mixing length scale
 242 (Thompson 2010; Stewart and Thompson 2016; Jansen et al. 2015, 2019; Kong and Jansen 2017).
 243 In studies focusing on continental shelves, Pringle (2001) and Brink (2017) used the topographic
 244 Rhines scale to represent the eddy wavelength. Jansen et al. (2015) and Grooms et al. (2015)
 245 suggested using the ‘effective’ Rhines scale, taking both planetary and topographic PV gradients
 246 into account by setting $|\nabla Q| = \left| \frac{f_0}{H} \nabla h_b + \beta_0 \hat{y} \right|$ in equation (15).

247 Taking $\kappa = 1/L_{\text{Rossby}}$ or $\kappa = 1/L_{\text{Rhines}}$ as estimates for the eddy wavenumber, (13) yields the
 248 following expressions for the eddy diffusivity:

$$\mathcal{K}_{\text{Rossby}} = \frac{\mathcal{K}_0}{1 + \frac{1}{\gamma^2} \frac{N^2 H^2}{f_0^2} \mathcal{A} |\nabla Q|^2} = \frac{\mathcal{K}_0}{1 + \frac{1}{\gamma^2} \mathcal{A} N^2 \alpha^2}, \quad (16)$$

$$\mathcal{K}_{\text{Rhines}} = \frac{\mathcal{K}_0}{1 + \frac{1}{\gamma^2} \mathcal{A} \mathcal{U} |\nabla Q|} = \frac{\mathcal{K}_0}{1 + \frac{1}{\gamma^2} \mathcal{A} \mathcal{U} \frac{|f_0|}{H} |\alpha|}. \quad (17)$$

249 With (16) and (17), we have two different analytical expressions for the cross-stream eddy diffusivity
 250 over a topographic slope, both of which indicate that topographic slopes suppress cross-isobath
 251 mixing. We proceed to test both expressions in a numerical model.

252 3. Validating theory in an idealized channel model

253 *a. Numerical model description*

254 We use the Bergen Layered Ocean Model (BLOM), the ocean component of the Norwegian
 255 Earth System Model (NorESM; Seland et al. 2020), in an idealized channel configuration. The
 256 simulations are described in Nummelin and Isachsen (2024) and we only give a brief summary
 257 here.

258 The model uses 51 isopycnal levels (potential density referenced to 2000 dbar) with a 2-level
 259 bulk mixed layer at the surface. The channel configuration is 416 km long in the zonal (x) direction
 260 and 1024 km wide in the meridional (y) direction with a 2 km resolution, and is re-entrant in the
 261 zonal direction. There are continental slopes of 2000 m extension from the shelf break at 250m
 262 to the bottom of the domain at 2250 m depth on both sides of the channel, centered at 150 km
 263 from the domain edge. To trigger instabilities we add white noise to the bottom topography with
 264 a standard deviation of 10 m. The channel is set up on the Northern Hemisphere f -plane. The
 265 model is initialized from rest with constant salinity and a horizontally homogeneous temperature
 266 profile. The density is determined by temperature alone, which has a maximum at the surface and
 267 decays exponentially towards the bottom. There is no buoyancy forcing (nor restoring) and we
 268 only force the flow with a constant westward wind stress. The surface mixed layer is kept shallow
 269 by parameterization of submesoscale mixed layer eddies (Fox-Kemper et al. 2008) that counter the
 270 vertical mixing induced by the constant wind forcing.

283 and 0.027. These values are fairly representative for continental slopes (LaCasce 2017). All
 284 simulations are spun up for 10 years, to a semi-equilibrium where the kinetic energy has stabilized
 285 but still has some variability. The model fields are then diagnosed over an additional 5-year period
 286 (between years 11–15). The parameter settings and experiments are laid out in Tables 1 and 2,
 287 respectively.

TABLE 1. BLOM model constants for the channel simulations.

Name	Symbol	Value
Wind stress	τ_x	0.05 N m^{-2}
Horiz. grid size	$\Delta x, \Delta y$	2 km
Baroclinic timestep	Δt	120 s
Domain x -size	L_x	416 km
Domain y -size	L_y	1024 km
Gravitational acceleration	g	9.806 m s^{-2}
Coriolis parameter	f_0	$1 \times 10^{-4} \text{ s}^{-1}$
Slope mid-point distance from domain edge	Y_S	150 km
Shelf depth	H_{Shelf}	250 m
Slope height	H_{Slope}	2000 m

288 TABLE 2. Channel model experiments. L_{Rossby} is the mean deformation radius (equation 14) averaged over the
 289 last 5 years of the 15-year long experiments in the central basin (where the bottom depth is larger than 2250 m).

Name	L_{Rossby}	Slope Width	Slope Magnitude
Exp 1	$34.1 \pm 1.3 \text{ km}$	75 km	0.027
Exp 2	$34.1 \pm 1.1 \text{ km}$	100 km	0.020
Exp 3	$34.4 \pm 1.0 \text{ km}$	125 km	0.016
Exp 4	$30.6 \pm 1.3 \text{ km}$	75 km	0.027
Exp 5	$30.6 \pm 1.2 \text{ km}$	100 km	0.020
Exp 6	$30.4 \pm 1.0 \text{ km}$	125 km	0.016
Exp 7	$24.9 \pm 1.2 \text{ km}$	75 km	0.027
Exp 8	$25.9 \pm 1.0 \text{ km}$	100 km	0.020
Exp 9	$24.9 \pm 1.0 \text{ km}$	125 km	0.016

290 *b. Computing diffusivities from the model data*

291 The goal is to compare cross-slope eddy diffusivities diagnosed from the model with the parame-
 292 terizations from equations (16) and (17). We diagnose diffusivities using the flux-gradient relation
 293 $\mathcal{F}_C = -\mathcal{K}\nabla C$. As (16) and (17) were derived for a barotropic model, we first average the model

variables over depth. Then, we make a Reynolds decomposition of the tracer and velocity fields in the zonal (re-entrant) direction. We denote zonal mean fields with angle brackets (e.g. $\langle v \rangle$) and the eddy field (deviations from the zonal mean) with stars (e.g. v^\star). Diagnosing eddy diffusivities over bottom topography is typically done using spatial filtering because standing waves due to topography don't get detected when using Reynolds averaging (e.g. Khani et al. 2019; Buzzicotti et al. 2023; Xie et al. 2023). However, in our simulations we only have smooth topographic slopes without corrugations, and hence no standing waves. Therefore we assume that using Reynolds averaging in the zonal direction is justified here.

The cross-stream (y-direction) diffusivity of a tracer C is diagnosed from the depth-averaged tracer and cross-stream velocity fields using the flux-gradient relation:

$$\mathcal{K}_{\text{diag}}^C = -\frac{\langle v^\star C^\star \rangle}{\partial \langle C \rangle / \partial y}. \quad (18)$$

In the computation of (18), we select only those data points where the absolute value of the gradient $\partial \langle C \rangle / \partial y$ is larger than a threshold value, to avoid problems with unphysical diffusivity values. The choice of the threshold value mainly affects the diffusivity over the flat bottom, where gradients can become very small, while the impact over the slopes is limited. From the diffusivity values computed using (18), we select only the positive values. For the final analysis, $\mathcal{K}_{\text{diag}}^C$ is averaged over time, so that it is only a function of the cross-channel coordinate y . Formally, the parameterizations apply only to passive tracers, deriving as they do from the Taylor diffusivity (equation 8). However, we lack passive tracers in the present model simulations. Therefore we determined $\mathcal{K}_{\text{diag}}$ using two different tracers: temperature and (shallow water) PV, i.e. $(f + \zeta)/H$ with ζ the relative vorticity. The resulting diagnosed diffusivities are denoted as $\mathcal{K}_{\text{diag}}^T$ and $\mathcal{K}_{\text{diag}}^{PV}$, respectively. Neither temperature nor PV are necessarily passive, although they can be in certain situations (e.g. Larichev and Held 1995). The results turn out to be relatively insensitive to the chosen tracer.

To apply equations (16) and (17) to calculate parameterized eddy diffusivities from the numerical model data, we need to determine the eddy kinetic energy \mathcal{U}^2 , the anisotropy factor \mathcal{A} , and the eddy decorrelation timescale γ . Both \mathcal{U}^2 and \mathcal{A} can be expressed in terms of the eddy velocity field. Firstly, \mathcal{U}^2 is given by equation (7). Secondly, following Wei and Wang (2021) and using the monochromatic wave expression (3) for the eddy streamfunction, we can write the anisotropy

factor \mathcal{A} as

$$\mathcal{A} = \frac{k^2}{k^2 + l^2} = \frac{\langle \psi_x'^2 \rangle}{\langle \psi_x'^2 \rangle + \langle \psi_y'^2 \rangle} = \frac{\langle v^{\star 2} \rangle}{\langle u^{\star 2} \rangle + \langle v^{\star 2} \rangle}. \quad (19)$$

It should be noted that most studies of mixing suppression assume that mesoscale eddies are horizontally isotropic, and hence that the anisotropy factor $\mathcal{A} = k^2/\kappa^2$ is equal to 1/2 everywhere (e.g. Ferrari and Nikurashin 2010; Naveira Garabato et al. 2011; Klocker et al. 2012; Chen et al. 2014, 2015; Griesel et al. 2015; Kong and Jansen 2017; Groeskamp et al. 2020). Wei and Wang (2021) concluded that eddies over topographic slopes are strongly anisotropic and as such that the anisotropy factor is important. We retain the term in our expression for \mathcal{K} for completeness and analyze its importance later.

With equations (7) and (19), the unsuppressed diffusivity \mathcal{K}_0 can be written as $\mathcal{K}_0 = \mathcal{A}\mathcal{U}^2/\gamma = \langle v^{\star 2} \rangle/\gamma$, and equations (16) and (17) become

$$\mathcal{K}_{\text{Rossby}} = \left(1 + \frac{1}{\gamma^2} \frac{\langle v^{\star 2} \rangle}{\langle u^{\star 2} \rangle + \langle v^{\star 2} \rangle} N^2 \alpha^2 \right)^{-1} \frac{\langle v^{\star 2} \rangle}{\gamma}, \quad (20)$$

$$\mathcal{K}_{\text{Rhines}} = \left(1 + \frac{1}{\gamma^2} \frac{\langle v^{\star 2} \rangle}{\sqrt{\langle u^{\star 2} \rangle + \langle v^{\star 2} \rangle}} \frac{|f_0|}{H} |\alpha| \right)^{-1} \frac{\langle v^{\star 2} \rangle}{\gamma}. \quad (21)$$

Expressions (20) and (21) are computed from the depth and zonally averaged velocity fields, and averaged over time for the final analysis. For N in equation (20), we use the depth-averaged buoyancy frequency. The last parameter remaining is γ , the inverse eddy velocity decorrelation timescale. This represents damping due to nonlinear eddy-eddy interactions, and is usually left as a tunable parameter. Klocker and Abernathey (2014) found a good fit for diffusivity at the surface for $\gamma^{-1} = 4$ days, and Groeskamp et al. (2020) found $\gamma^{-1} = 1.68$ days for full-depth estimates. We explore the sensitivity of the parameterizations to γ subsequently.

c. Comparing parameterized and diagnosed diffusivities

Figure 2 shows the diagnosed and parameterized cross-slope diffusivities across the channel for all 9 experiments (Table 2). The diagnosed diffusivities $\mathcal{K}_{\text{diag}}^T$ and $\mathcal{K}_{\text{diag}}^{PV}$ are shown by the continuous and dashed black lines, respectively. Over the topographic slopes (gray shaded areas)

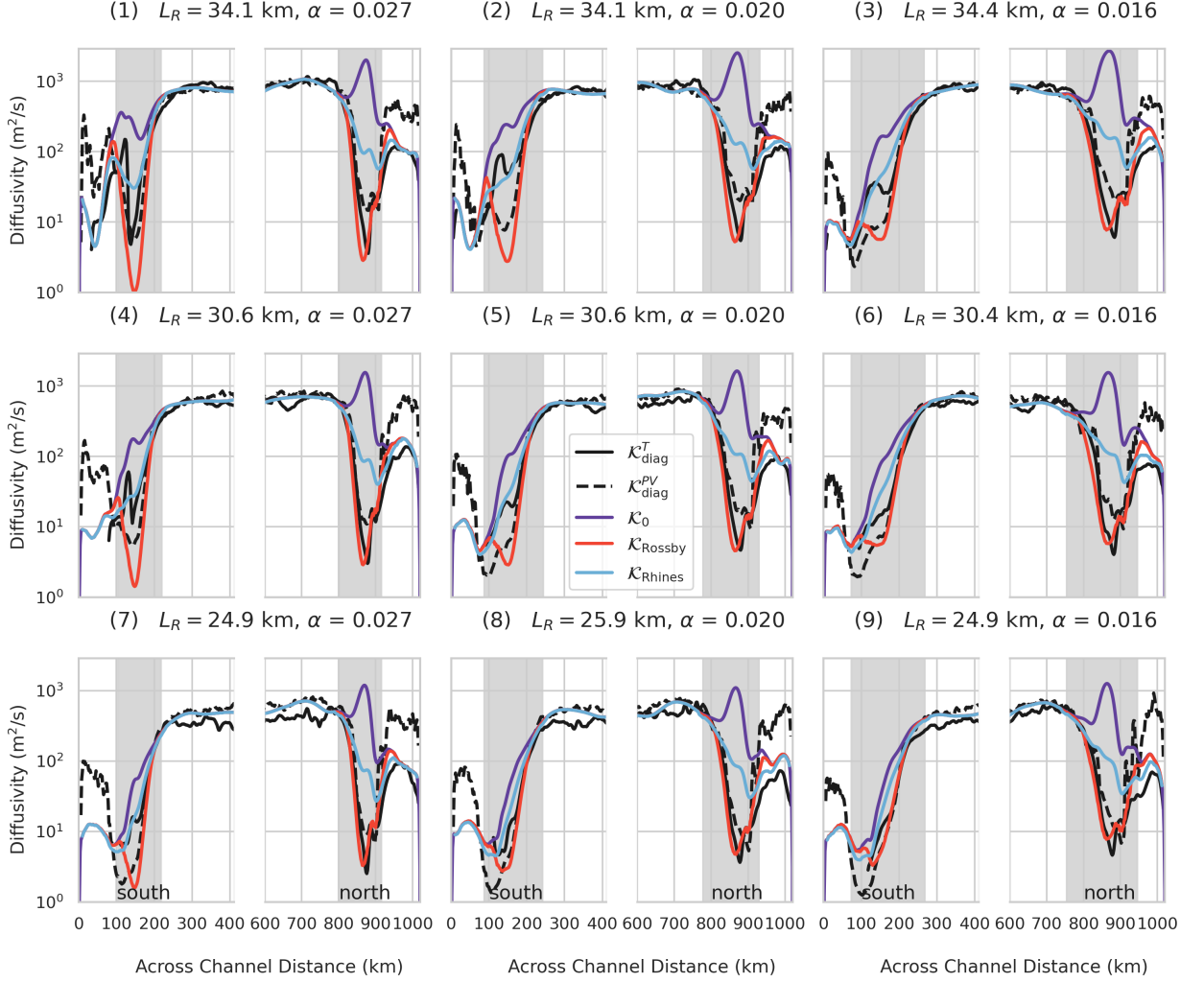


FIG. 2. Zonal and time mean depth-averaged cross-slope diffusivities across the channel for all 9 experiments from Table 2. Diffusivities are all plotted on a logarithmic scale. The continuous black line shows the diagnosed temperature diffusivity; the dashed black line shows the diagnosed PV diffusivity; the purple line shows the parameterized unsuppressed diffusivity from equation (10); the red and blue lines show the parameterized diffusivities from equations (20) and (21), respectively. The parameterized diffusivities are all shown for $\gamma^{-1} = 4$ days. The mid-basin part between 400 and 600 km is not shown; here the diffusivity is approximately constant. The gray shaded areas indicate the topographic slopes.

they are suppressed compared to the flat mid-basin by 2–3 orders of magnitude. Over the northern (prograde) slope, $\mathcal{K}_{\text{diag}}^T$ and $\mathcal{K}_{\text{diag}}^{PV}$ are very similar across all experiments; over the southern (retrograde) slope they exhibit differences for some experiments, with $\mathcal{K}_{\text{diag}}^T$ showing local maxima.

353 The reason for this is that the wind forcing induces northward Ekman transport, so that the cross-
 354 channel temperature gradient $\partial T/\partial y$ becomes small in the south, hence $\mathcal{K}_{\text{diag}}^T$ becomes large
 355 (equation 18).

356 Next, the purple, red and blue lines show the parameterized diffusivities \mathcal{K}_0 , $\mathcal{K}_{\text{Rossby}}$ and $\mathcal{K}_{\text{Rhines}}$,
 357 respectively. Each of these employ $\gamma^{-1} = 4$ days; this produces good agreement between the
 358 parameterized and diagnosed diffusivities in the mid-basin, but we will discuss the impact of γ
 359 below. Looking first at the parameterized unsuppressed diffusivity \mathcal{K}_0 (equation 10), we see that it
 360 is weaker in the south than in the mid-basin, but overestimates $\mathcal{K}_{\text{diag}}^T$ there. Over the northern slope,
 361 \mathcal{K}_0 has a maximum, and becomes even stronger than in the mid-basin. The reason is that eddy
 362 kinetic energy is enhanced over the northern slope (not shown). Focusing on our parameterizations
 363 that account for topographic PV gradients, $\mathcal{K}_{\text{Rossby}}$ and $\mathcal{K}_{\text{Rhines}}$, we see that both are suppressed
 364 over the slopes and are much better approximations of the diagnosed diffusivity. Over the southern
 365 (retrograde) slope, $\mathcal{K}_{\text{Rhines}}$ matches well with $\mathcal{K}_{\text{diag}}^T$, whereas $\mathcal{K}_{\text{Rossby}}$ is closer to $\mathcal{K}_{\text{diag}}^{PV}$. Over the
 366 northern (prograde) slope, $\mathcal{K}_{\text{Rhines}}$ overestimates both diagnosed diffusivities, while $\mathcal{K}_{\text{Rossby}}$ closely
 367 follows the profile of $\mathcal{K}_{\text{diag}}^T$. The reduction by 2–3 orders of magnitude of the diagnosed diffusivity
 368 over the slopes is captured by both $\mathcal{K}_{\text{Rossby}}$ and $\mathcal{K}_{\text{Rhines}}$ over the southern slope and by $\mathcal{K}_{\text{Rossby}}$
 369 over the northern slope. So, despite the QG assumptions not being valid everywhere in the present
 370 model setting (e.g. $|h_b| \ll H$), our parameterizations still produce results that are in fairly good
 371 agreement with the diagnosed diffusivity behavior.

375 Figure 3 explores the relevance of the anisotropy factor \mathcal{A} in the parameterized diffusivities.
 376 The value of \mathcal{A} changes from 0.6 (close to isotropic) over the flat mid-basin to 0.1 (0.2) over
 377 the northern (southern) slopes. Although this is a notable change, it is still small compared to
 378 the observed 2–3 orders of magnitude change in diffusivities over the slopes. In other words, it
 379 is the presence of α rather than \mathcal{A} in the suppression factor that is responsible for most of the
 380 suppression over the slopes. Figure 3 shows that using constant or non-constant \mathcal{A} yields very
 381 similar diffusivity profiles for experiment 8 from Table 2; this result holds across all experiments.

385 Figure 4 shows the profiles of the parameterized diffusivities $\mathcal{K}_{\text{Rossby}}$ and $\mathcal{K}_{\text{Rhines}}$ for a wide range
 386 of values of the eddy decorrelation timescale γ^{-1} . The dependence on γ is strongest for small γ^{-1} ,
 387 whereas it becomes weak for large γ^{-1} . We see that the value of γ^{-1} that gives the best agreement
 388 differs between the two parameterizations and also between the northern slope, southern slope

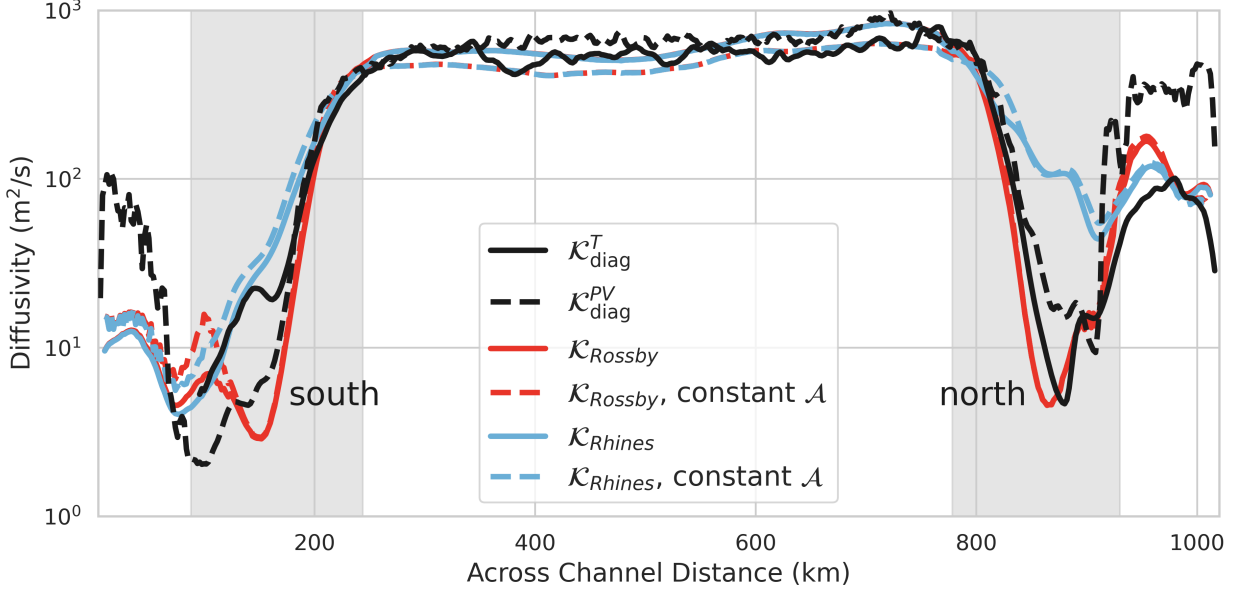


FIG. 3. Diagnosed and parameterized diffusivities (as in Figure 2) for experiment 5 from Table 2. Diffusivities are all plotted on a logarithmic scale. The dashed lines show the parameterized diffusivities with a constant anisotropy factor \mathcal{A} , taken to be the mean cross-basin value.

and flat-bottomed mid-basin. For small values of γ^{-1} , the parameterizations underestimate the diagnosed diffusivities in the mid-basin but overestimate diffusivities over the northern slope, with $\mathcal{K}_{\text{Rhines}}$ showing local maxima over the northern slope, approaching \mathcal{K}_0 (Figure 2). For larger values of γ^{-1} , the parameterized diffusivity profiles converge, but overestimate the diagnosed diffusivities in the mid-basin. $\mathcal{K}_{\text{Rossby}}$ matches best with the diagnosed diffusivities for values of γ^{-1} around 2–4 days. On the other hand, $\mathcal{K}_{\text{Rhines}}$ is relatively insensitive to the value of γ^{-1} over the southern slope, but performs best for high values of γ^{-1} over the northern slope. Note the exact value of γ^{-1} will vary depending on approximations, e.g. neglecting factors of π in the various expressions for length and time scales.

4. Discussion

a. Relevance of eddy length and time scales

In the derivation of (12), it is assumed that mesoscale eddies can be described as monochromatic waves with all energy at a single wavenumber. In reality, the oceanic eddy field contains motions

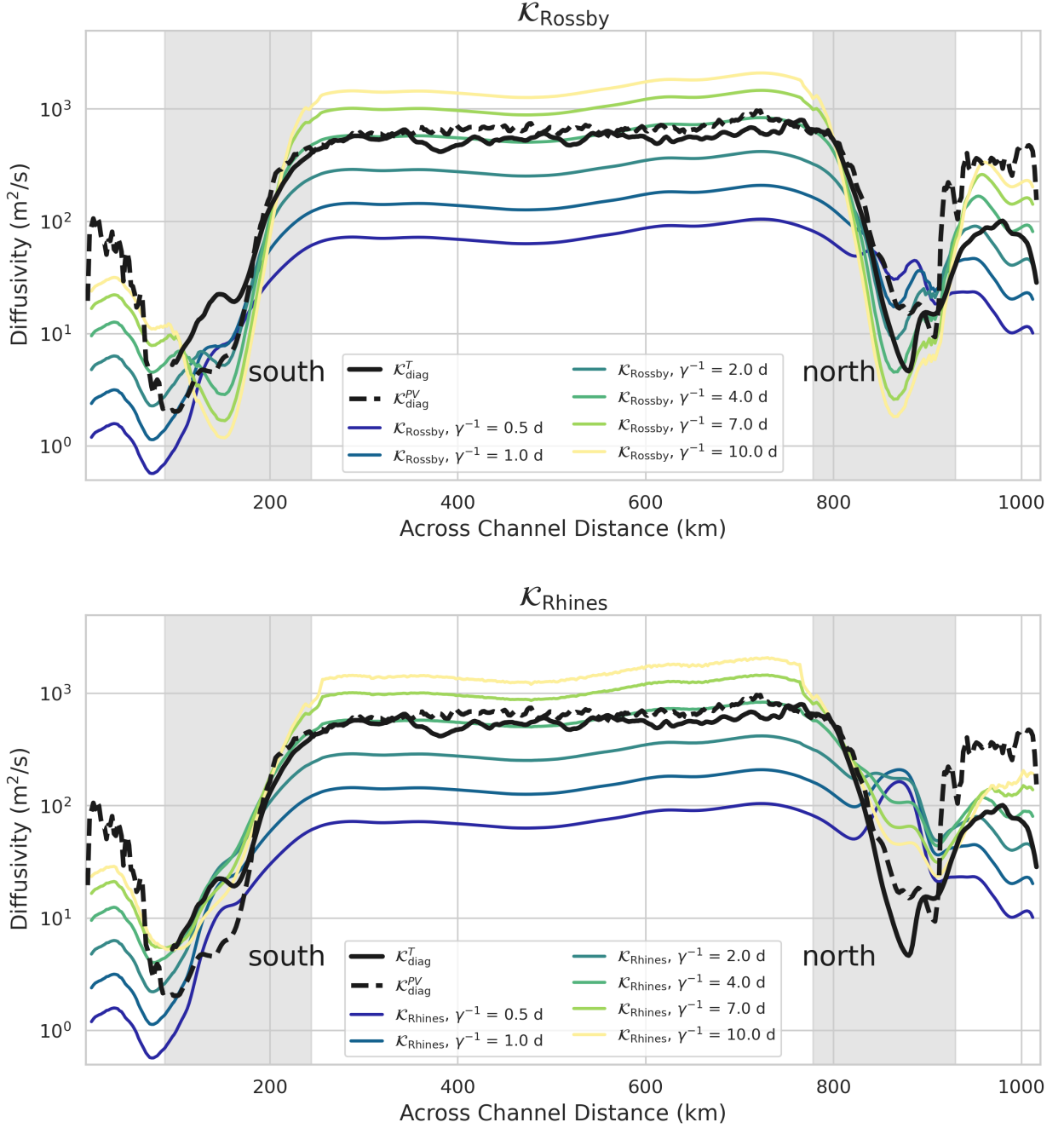


FIG. 4. Parameterized diffusivities $\mathcal{K}_{\text{Rossby}}$ (equation 20) and $\mathcal{K}_{\text{Rhines}}$ (equation 21) for different values of γ and diagnosed diffusivities $\mathcal{K}_{\text{diag}}^T$ and $\mathcal{K}_{\text{diag}}^{PV}$, shown for experiment 5 from Table 2. The values of γ^{-1} are indicated in days. Diffusivities are all plotted on a logarithmic scale.

over a broad range of wavenumbers (Wunsch 2010; Wortham and Wunsch 2014). A number of studies have derived eddy diffusivity parameterizations for multichromatic waves. Chen et al. (2015)

404 developed a multi-wavenumber theory for eddy diffusivities, but only considered wavenumbers
 405 in the along-stream direction. Kong and Jansen (2017) considered the full two-dimensional EKE
 406 spectrum to compute eddy diffusivities, but assumed isotropy. Instead, like most other studies, we
 407 retained the assumption of monochromatic waves. We considered two different length scales to set
 408 the dominant wavelength: the Rossby radius and the topographic Rhines scale. As seen in Figure
 409 2, we find good agreement between theory and model results in both cases. This suggests that the
 410 assumption of monochromatic waves works well with a realistic value for the most energetic eddy
 411 length scale for this model.

412 Other studies have not yet provided a clear conclusion on which length scale best represents eddy
 413 mixing length over topographic slopes. Wang and Stewart (2020) and Wei et al. (2022) found that
 414 the topographic Rhines scale works well to parameterize eddy diffusivity over retrograde slopes,
 415 but that it is not suitable for prograde slopes in a stratified ocean. On the other hand, Wei and
 416 Wang (2021) parameterized diffusivities over retrograde slopes using the Rossby radius, and found
 417 that the topographic Rhines scale led to an overestimation of the diagnosed diffusivity. These
 418 findings suggest differences in eddy length scales between prograde and retrograde slopes. In our
 419 simulations, a relevant difference between the two slopes is that EKE is enhanced over the northern
 420 (prograde) slope due to Ekman downwelling, but weakened in the south due to Ekman upwelling.
 421 Over the southern (retrograde) slope, the suppression of the eddy diffusivity is already captured
 422 quite well by \mathcal{K}_0 , which takes into account EKE but not topographic PV gradients. Hence, in
 423 this upwelling region, the weakened EKE already contains a large part of the suppression. On the
 424 other hand, over the northern (prograde) slope the topographic PV gradient is needed to represent
 425 the suppression effect. Here, an important difference between the two length scales is that $\mathcal{K}_{\text{Rhines}}$
 426 is inversely proportional to the PV gradient, whereas $\mathcal{K}_{\text{Rossby}}$ is inversely proportional to the PV
 427 gradient squared. The importance of the squared PV gradient (the bottom slope) was noted in
 428 Nummelin and Isachsen (2024) and previous studies, suggesting that the Rossby radius might be
 429 the more appropriate length scale to use. This will be further discussed in Section 4b. Finally, in the
 430 simulations used in this study, the eddies have a size in the order of the Rossby radius (not shown),
 431 whereas the topographic Rhines scale is an order of magnitude too small. This further supports the
 432 conclusion that the Rossby radius is the appropriate eddy length scale for the simulations presented
 433 here.

Regarding the eddy velocity decorrelation timescale, there are, to the best of our knowledge, no observational studies on the values of γ in the ocean. As noted, γ is typically left as an adjustable parameter when computing eddy diffusivities (e.g. Klocker and Abernathey 2014; Groeskamp et al. 2020). The value of γ could possibly be inferred from an inverse method, like that employed in Mak et al. (2022a) for the mesoscale eddy energy dissipation timescale. Another option could be to determine γ from the autocorrelation of observational velocity timeseries. Our results suggest γ varies depending on the relevant dynamics in a region, and this should be examined further.

b. Relation with empirical expressions for eddy diffusivity

Among others, Brink (2012), Brink and Cherian (2013), Brink (2016) and Wei et al. (2022) have constructed an empirical scaling for eddy diffusivity in terms of the slope Burger number, $S = \alpha N / f_0$. They all give parameterizations for \mathcal{K} of the form

$$\mathcal{K} = \frac{\mu}{1 + \eta S^\varepsilon}, \quad S = \frac{\alpha N}{f_0}. \quad (22)$$

The values of the parameters μ and η and the exponent ε vary between these studies. The general form of (22) is the same as our expression for $\mathcal{K}_{\text{Rossby}}$, equation (16), if the factor f_0 in S is replaced by the eddy decorrelation timescale γ . The exponent ε in our case is equal to 2, which is the same as in Brink and Cherian (2013) and Brink (2016) (by contrast, Brink (2012) found $\varepsilon = 1$, whereas Wei et al. (2022) reported $\varepsilon = 1.4$). This means that our parameterization using the Rossby radius, which is dynamically based, is consistent with the previously found empirically based expressions for eddy diffusivities over topographic slopes.

c. Challenges for implementation in coarse-resolution climate models

One of the main reasons to study eddy diffusivities over topographic slopes is to create better parameterizations for coarse-resolution climate models. Using (13) with the appropriate length scale to compute eddy diffusivities requires knowledge on the eddy kinetic energy \mathcal{U}^2 , the eddy anisotropy factor \mathcal{A} , and the eddy velocity decorrelation timescale γ . Here we expressed \mathcal{U}^2 and \mathcal{A} in terms of the eddy velocity field and used the resulting expressions (20) and (21) to compute eddy diffusivities from the numerical model's depth-averaged flow field data, leaving γ as an adjustable parameter (Section 3b). However, expressions (20) and (21) are not suitable for implementation

in climate models. The reason is the lack of closures for the eddy-related parameters \mathcal{U}^2 , \mathcal{A} and γ , which depend on properties below the typical grid scale of coarse-resolution climate models. Closures and parameterizations of eddy kinetic energy are an active research topic (e.g. Eden and Greatbatch 2008; Jansen et al. 2015, 2019; Mak et al. 2017, 2018; Juricke et al. 2020a,b). Wei and Wang (2021) present a parameterization for the anisotropy factor, though the derivation is empirical. Note, though, that in our simulations, it is the topographic PV gradient rather than the anisotropy factor that causes most of the suppression of the depth-averaged diffusivity (see also Nummelin and Isachsen 2024). It is therefore a reasonable approximation to simplify the expressions by assuming a constant anisotropy factor. Regarding the eddy decorrelation timescale, more research is needed for determining prognostic equations for γ , as discussed in Section 4a. Furthermore, a shortcoming of the parameterizations presented here is that they do not take into account baroclinic effects and hence cannot be used to get vertical profiles of the eddy diffusivity. Adding stratification greatly increases the complexity of the problem, which can already be seen in a two-layer model (e.g. Straub 1994; Boland et al. 2012). Moreover, a varying anisotropy factor might be important for the vertical structure of eddy diffusivities (Stewart et al. 2015; Wei and Wang 2021), so assuming constant anisotropy is then no longer a good approximation. Nevertheless, with appropriate estimates for \mathcal{U}^2 , \mathcal{A} , and γ , we still consider expression (13) of value for testing in climate models to represent depth-averaged eddy diffusivities.

d. Applicability of results for observations

The skill of parameterizations (20) and (21) in reproducing eddy diffusivities in a numerical model also motivates application to observational data. Direct observations of mesoscale eddy mixing can be made in tracer release experiments (Ledwell et al. 1993, 1998; Tulloch et al. 2014; Zika et al. 2020; Bisits et al. 2023), but these experiments are expensive and labor intensive, and only provide information about a specific region. By contrast, our parameterizations could be used to infer eddy diffusivity values from more easily attainable observations. Groeskamp et al. (2020) applied the velocity formulation from Ferrari and Nikurashin (2010) to an observation-based gridded ocean climatology to create full-depth global estimates of eddy diffusivities. However, the expression of Ferrari and Nikurashin (2010) does not include effects of topographic PV gradients. Moreover, it requires fitting of the eddy decorrelation timescale γ , and approximating the total

eddy phase speed c_w . Table 4 of Wei and Wang (2021) summarizes the methods that different studies used to determine c_w , which include empirical fits to numerical model results (e.g. Klocker et al. 2012; Pennel and Kamenkovich 2014), linear stability analysis (e.g. Eden 2011; Griesel et al. 2015), the use of SSH measurements (e.g. Ferrari and Nikurashin 2010; Naveira Garabato et al. 2011; Sallée et al. 2011; Abernathey and Marshall 2013; Bates et al. 2014; Klocker and Abernathey 2014; Balwada et al. 2016; Roach et al. 2016, 2018; Bolton et al. 2019; Busecke and Abernathey 2019; Groeskamp et al. 2020), or simply assuming $c_w \approx 0$ (e.g. Meredith et al. 2012; Bire and Wolfe 2018). By contrast, in the PV formulation the term $c_w - U$ is replaced by c , the intrinsic eddy phase speed, for which we have an analytical expression in terms of the background (planetary and topographic) PV gradient. Thus, in the barotropic case we can calculate c in a straightforward way from β and the topographic slope, and circumvent the problem of having to determine c_w . In the end, the only observational measurements that our equations (20) and (21) require are information on stratification, topographic slopes, and flow velocity timeseries (for \mathcal{A} , \mathcal{U}^2 and γ); one could obtain these from mooring data. Within the assumptions made here, this provides a new and improved method to estimate depth-averaged eddy diffusivities based on oceanographic measurements, and thus to study variability in eddy diffusivity across the ocean.

5. Summary and Conclusion

We derived an analytical expression, equation (13), to describe depth-averaged eddy diffusivities over topographic slopes (Figure 2). This expression is a specific case of the general equation (12) for the cross-stream eddy diffusivity in the presence of a background PV gradient. Equation (12) explicitly links eddy diffusivity to the PV gradient (Nakamura and Zhu 2010b), thus providing a PV formulation of mixing suppression, as opposed to the velocity formulation (9) presented in previous studies (e.g. Ferrari and Nikurashin 2010; Klocker et al. 2012). An advantage of the PV formulation is that it does not require information on c_w , the Doppler-shifted or apparent phase speed of the eddies, and U , the background mean flow. We circumvent the problem of having to determine c_w and U and instead keep an analytical expression for the intrinsic eddy phase speed, which is linked to the PV gradient. Furthermore, keeping the PV gradient ∇Q in the expression for \mathcal{K} , we can substitute exact expressions for ∇Q to see which physical mechanisms determine \mathcal{K} . Many studies on mixing suppression in the ACC assume the PV gradient is set by planetary

518 β (e.g. Ferrari and Nikurashin 2010; Naveira Garabato et al. 2011; Klocker et al. 2012; Griesel
519 et al. 2015). Instead, the main focus of this study was the influence of bottom topography on
520 eddy mixing. Across the world’s oceans the topographic PV gradient is typically larger than the
521 planetary PV gradient (with the exception of low latitudes). Equation (13) directly relates the
522 eddy diffusivity to the topographic slope α . This equation is not based on empirical fits to model
523 results, but on physically consistent derivations that include topography from the start. Finally,
524 our parameterization can be calculated from velocity timeseries, presenting a new opportunity for
525 computing eddy diffusivities from observational data.

526 A number of issues still remain to be addressed. Closures for the eddy anisotropy, EKE, and
527 decorrelation timescale are missing; the physical mechanisms setting the eddy length scale in
528 different dynamical regimes require further study; and the parameterizations for \mathcal{K} presented in
529 this study do not take into account baroclinic effects. Nevertheless, the parameterizations help in
530 understanding the physical mechanism of mixing suppression by topography, and can accurately
531 represent depth-averaged eddy diffusivities in an idealized simulation. This motivates future
532 studies to extend the parameterizations to a baroclinic (depth-varying) framework, and to explore
533 the applicability of the parameterizations for computing eddy diffusivities from observations and
534 models.

535 *Author contributions.* **MFS:** Conceptualization, Methodology, Formal analysis, Writing - Orig-
536 inal Draft. **JHL:** Conceptualization, Methodology. **SG:** Conceptualization, Methodology, Super-
537 vision, Project administration, Funding acquisition. **AN:** Software, Formal analysis, Resources.
538 **PEI:** Resources. **MLJB:** Supervision, Project administration, Funding acquisition. **Everyone:**
539 Writing - Review & Editing.

540 *Acknowledgments.* MFS was funded by the UU-NIOZ project “The intermittency of large-scale
541 ocean mixing” (project number NZ4543.3). JHL was supported under project number 302743 (the
542 Rough Ocean) of the Norwegian Research Council. AN and PEI were funded by the two Research
543 Council of Norway projects KeyClim (295046) and TopArctic (314826). MLJB was funded by
544 the program of the Netherlands Earth System Science Centre (NESSC), financially supported by
545 the Ministry of Education, Culture and Science (OCW, grant number 024.002.001). The model
546 simulations and storage were performed on resources provided by Sigma2 - the National Infrastruc-
547 ture for High Performance Computing and Data Storage in Norway under the accounts NN9252K,
548 NS9252K, NN9869K, and NS9869K. We thank Julian Mak and one anonymous reviewer for their
549 thorough and helpful reviews of the manuscript.

550 *Data availability statement.* The model configuration and namelists needed for reproducing the
551 results are published in Zenodo (Nummelin 2023b) and available at [https://doi.org/10.5281/](https://doi.org/10.5281/zenodo.8227381)
552 [zenodo.8227381](https://doi.org/10.5281/zenodo.8227381). The key model outputs (Nummelin 2023a) needed for reproducing the analysis
553 are published at the NIRD research data archive and available at [https://archive.sigma2.no/](https://archive.sigma2.no/pages/public/datasetDetail.jsf?id=10.11582/2023.00129)
554 [pages/public/datasetDetail.jsf?id=10.11582/2023.00129](https://archive.sigma2.no/pages/public/datasetDetail.jsf?id=10.11582/2023.00129). Scripts for data processing
555 and plotting can be shared upon request.

Derivation of expression for cross-stream eddy diffusivity

To compute the cross-stream eddy diffusivity, we need an analytical expression for the eddy streamfunction ψ' . We express ψ' as a Rossby wave (equation 3). Combining equations (4) and (6), we get a differential equation for the wave amplitude $a(t)$:

$$\frac{da}{dt} + (\gamma + ikc_w)a \equiv \frac{da}{dt} + \lambda a = Ar(t). \quad (\text{A1})$$

To solve (A1), we use an integrating factor $e^{\lambda t}$:

$$\left(\frac{da}{dt} + \lambda a \right) e^{\lambda t} = \frac{d}{dt} \left(a(t) e^{\lambda t} \right) = Ar(t) e^{\lambda t}. \quad (\text{A2})$$

For a full solution, we need an initial condition. For this, we assume that we started out in a state of rest, i.e. $\lim_{t \rightarrow -\infty} a(t) = 0$. This gives us the solution

$$a(t) = A \int_{-\infty}^t r(\tau) e^{\lambda(\tau-t)} d\tau. \quad (\text{A3})$$

Now we need to determine the forcing amplitude A . We do this using the eddy kinetic energy (EKE), given by

$$\text{EKE} = \frac{1}{2} \langle u'^2 + v'^2 \rangle = \frac{1}{2} \langle |\psi'_x|^2 + |\psi'_y|^2 \rangle = \frac{1}{2} \langle \kappa^2 |\psi'|^2 \rangle = \frac{1}{2} \langle \kappa^2 |a|^2 \rangle \equiv \frac{1}{2} \mathcal{U}^2, \quad (\text{A4})$$

where $\langle \cdot \rangle$ denotes a time average. Using expression (A3) for $a(t)$, we find

$$|a|^2 = aa^* = A^2 \int_{-\infty}^t \int_{-\infty}^t r(\tau) r^*(\tau') e^{\lambda(\tau-t) + \lambda^*(\tau'-t)} d\tau d\tau', \quad (\text{A5})$$

where $*$ denotes complex conjugate. Since $r(t)$ is a white noise random process, $\langle r(\tau) r^*(\tau') \rangle = \delta(\tau - \tau')$. Furthermore, $\lambda \equiv \gamma + ikc_w$, so $\lambda + \lambda^* = 2\gamma$. This yields

$$\langle |a|^2 \rangle = A^2 \int_{-\infty}^t e^{2\gamma(\tau-t)} d\tau = \frac{A^2}{2\gamma}. \quad (\text{A6})$$

Combining this with the expression for the EKE, (A4), gives an expression for the stochastic forcing amplitude A :

$$A = \frac{\sqrt{2\gamma}\mathcal{U}}{\kappa}. \quad (\text{A7})$$

Combining equations (3), (A3) and (A7) gives us the following expression for the eddy stream-function:

$$\psi'(x, y, t) = \text{Re} \left(\frac{\sqrt{2\gamma}}{\kappa} \mathcal{U} e^{ikx+ily} \int_{-\infty}^t r(\tau) e^{\lambda(\tau-t)} d\tau \right). \quad (\text{A8})$$

We can use (A8) to get an expression for v' , which is needed to compute the Taylor diffusivity, given by equation (8). We approximate the Lagrangian velocity v_L with the Eulerian velocity of a particle advected by the mean flow (leaving out Re for simplicity in the notation):

$$v_L(t; x, y, 0) = v'(x + Ut, y, t) = \frac{\partial \psi'}{\partial x} \Big|_{(x+Ut, y, t)} = a(t) i k e^{ik(x+Ut)+ily}. \quad (\text{A9})$$

The autocorrelation of the cross-stream Lagrangian velocity R_{vv} is now given by

$$R_{vv} = \frac{2\gamma\mathcal{U}^2 k^2}{\kappa^2} e^{ikU(t-t')-\lambda t-\lambda^* t'} \int_{-\infty}^t \int_{-\infty}^{t'} r(\tau) r^*(\tau') e^{\lambda\tau+\lambda^*\tau'} d\tau' d\tau. \quad (\text{A10})$$

When taking the average $\langle R_{vv} \rangle$, as is needed for (8), we can again use that $\langle r(\tau) r^*(\tau') \rangle = \delta(\tau - \tau')$. This gives us

$$\langle R_{vv} \rangle = \frac{2\gamma\mathcal{U}^2 k^2}{\kappa^2} e^{ikU(t-t')-\lambda t-\lambda^* t'} \int_{-\infty}^t \int_{-\infty}^{t'} \delta(\tau - \tau') e^{\lambda\tau+\lambda^*\tau'} d\tau' d\tau. \quad (\text{A11})$$

The solution to the integral is (using that $\lambda + \lambda^* = 2\gamma$):

$$\int_{-\infty}^t \int_{-\infty}^{t'} \delta(\tau - \tau') e^{\lambda\tau+\lambda^*\tau'} d\tau' d\tau = \frac{1}{2\gamma} \left[\theta(t' - t) \left(e^{2\gamma t} - e^{2\gamma t'} \right) + e^{2\gamma t'} \right], \quad (\text{A12})$$

where θ is the Heaviside step function (equal to zero for negative arguments and to one for positive arguments). In (8) we integrate over t' from 0 to t , meaning that t' must be smaller than t . So

582 $\theta(t' - t) = 0$, and (A12) reduces to

$$\int_{-\infty}^t \int_{-\infty}^{t'} \delta(\tau - \tau') e^{\lambda\tau + \lambda^* \tau'} d\tau' d\tau = \frac{1}{2\gamma} e^{2\gamma t'}. \quad (\text{A13})$$

583 So (A11) becomes

$$\langle R_{vv} \rangle = \frac{\mathcal{U}^2 k^2}{\kappa^2} e^{ik(c_w - U)(t' - t)} e^{\gamma(t' - t)}, \quad (\text{A14})$$

584 where we used $\lambda = \gamma + ikc_w$ and $c_w = U + c$. Now we integrate over the real part of $\langle R_{vv} \rangle$ to compute
585 the diffusivity as in (8):

$$\mathcal{K} = \lim_{t \rightarrow \infty} \frac{\mathcal{U}^2 k^2}{\kappa^2} \int_0^t e^{\gamma(t' - t)} \cos[k(c_w - U)(t' - t)] dt'. \quad (\text{A15})$$

586 We can solve this integral using the substitution $\sigma = t' - t$ (and $c_w - U = c$):

$$\mathcal{K} = \lim_{t \rightarrow \infty} \frac{\mathcal{U}^2 k^2}{\kappa^2 (\gamma^2 + c^2 k^2)} \left[\gamma - e^{-\gamma t} (\gamma \cos(ckt) - ck \sin(ckt)) \right]. \quad (\text{A16})$$

587 Finally we take the limit of $t \rightarrow \infty$ to find the diffusivity in an equilibrium situation:

$$\mathcal{K} = \frac{k^2}{\kappa^2} \frac{\gamma \mathcal{U}^2}{\gamma^2 + c^2 k^2} = \frac{k^2}{\kappa^2} \frac{\gamma \mathcal{U}^2}{\gamma^2 + (c_w - U)^2 k^2} = \frac{\mathcal{A} \mathcal{U}^2 / \gamma}{1 + \frac{k^2}{\gamma^2} (c_w - U)^2}. \quad (\text{A17})$$

References

- Abernathey, R. P., and J. Marshall, 2013: Global surface eddy diffusivities derived from satellite altimetry. *Journal of Geophysical Research: Oceans*, **118** (2), 901–916, <https://doi.org/10.1002/jgrc.20066>.
- Balwada, D., K. G. Speer, J. H. LaCasce, W. B. Owens, J. Marshall, and R. Ferrari, 2016: Circulation and Stirring in the Southeast Pacific Ocean and the Scotia Sea Sectors of the Antarctic Circumpolar Current. *Journal of Physical Oceanography*, **46** (7), 2005–2027, <https://doi.org/10.1175/JPO-D-15-0207.1>.
- Bates, M., R. Tulloch, J. Marshall, and R. Ferrari, 2014: Rationalizing the Spatial Distribution of Mesoscale Eddy Diffusivity in Terms of Mixing Length Theory. *Journal of Physical Oceanography*, **44** (6), 1523–1540, <https://doi.org/10.1175/JPO-D-13-0130.1>.
- Bire, S., and C. L. P. Wolfe, 2018: The Role of Eddies in Buoyancy-Driven Eastern Boundary Currents. *Journal of Physical Oceanography*, **48** (12), 2829–2850, <https://doi.org/10.1175/JPO-D-18-0040.1>.
- Bisits, J. I., G. J. Stanley, and J. D. Zika, 2023: Can We Accurately Quantify a Lateral Diffusivity from a Single Tracer Release? *Journal of Physical Oceanography*, **53** (2), 647–659, <https://doi.org/10.1175/JPO-D-22-0145.1>.
- Boland, E. J. D., A. F. Thompson, E. Shuckburgh, and P. H. Haynes, 2012: The Formation of Nonzonal Jets over Sloped Topography. *Journal of Physical Oceanography*, **42** (10), 1635–1651, <https://doi.org/10.1175/JPO-D-11-0152.1>.
- Bolton, T., R. Abernathey, and L. Zanna, 2019: Regional and Temporal Variability of Lateral Mixing in the North Atlantic. *Journal of Physical Oceanography*, **49** (10), 2601–2614, <https://doi.org/10.1175/JPO-D-19-0042.1>.
- Brink, K. H., 2012: Baroclinic instability of an idealized tidal mixing front. *Journal of Marine Research*, **70** (4), 661–688, <https://doi.org/10.1357/002224012805262716>.
- Brink, K. H., 2016: Continental Shelf Baroclinic Instability. Part I: Relaxation from Upwelling or Downwelling. *Journal of Physical Oceanography*, **46** (2), 551–568, <https://doi.org/10.1175/JPO-D-15-0047.1>.

- 616 Brink, K. H., 2017: Surface Cooling, Winds, and Eddies over the Continental Shelf. *Journal of*
617 *Physical Oceanography*, **47** (4), 879–894, <https://doi.org/10.1175/JPO-D-16-0196.1>.
- 618 Brink, K. H., and D. A. Cherian, 2013: Instability of an idealized tidal mixing front: Symmetric
619 instabilities and frictional effects. *Journal of Marine Research*, **71** (6), 425–450, [https://doi.org/](https://doi.org/10.1357/002224013812587582)
620 [10.1357/002224013812587582](https://doi.org/10.1357/002224013812587582).
- 621 Busecke, J. J. M., and R. P. Abernathey, 2019: Ocean mesoscale mixing linked to climate variability.
622 *Science Advances*, **5** (1), eaav5014, <https://doi.org/10.1126/sciadv.aav5014>.
- 623 Buzzicotti, M., B. A. Storer, H. Khatri, S. M. Griffies, and H. Aluie, 2023: Spatio-Temporal Coarse-
624 Graining Decomposition of the Global Ocean Geostrophic Kinetic Energy. *Journal of Advances*
625 *in Modeling Earth Systems*, **15** (6), e2023MS003693, <https://doi.org/10.1029/2023MS003693>.
- 626 Canuto, V. M., Y. Cheng, A. M. Howard, and M. S. Dubovikov, 2019: Three-Dimensional,
627 Space-Dependent Mesoscale Diffusivity: Derivation and Implications. *Journal of Physical*
628 *Oceanography*, **49** (4), 1055–1074, <https://doi.org/10.1175/JPO-D-18-0123.1>.
- 629 Chapman, C., and J.-B. Sallée, 2017: Isopycnal Mixing Suppression by the Antarctic Circumpo-
630 lar Current and the Southern Ocean Meridional Overturning Circulation. *Journal of Physical*
631 *Oceanography*, **47** (8), 2023–2045, <https://doi.org/10.1175/JPO-D-16-0263.1>.
- 632 Charney, J. G., 1947: The Dynamics of Long Waves in a Baroclinic Westerly Current. *Journal of*
633 *Meteorology*, **4** (5), 136–162, [https://doi.org/10.1175/1520-0469\(1947\)004<0136:TDOLWI>2.](https://doi.org/10.1175/1520-0469(1947)004<0136:TDOLWI>2.0.CO;2)
634 [0.CO;2](https://doi.org/10.1175/1520-0469(1947)004<0136:TDOLWI>2.0.CO;2).
- 635 Chelton, D. B., R. A. deSzoeke, M. G. Schlax, K. El Naggar, and N. Siwertz, 1998: Ge-
636 ographical Variability of the First Baroclinic Rossby Radius of Deformation. *Journal of*
637 *Physical Oceanography*, **28** (3), 433–460, [https://doi.org/10.1175/1520-0485\(1998\)028<0433:](https://doi.org/10.1175/1520-0485(1998)028<0433:GVOTFB>2.0.CO;2)
638 [GVOTFB>2.0.CO;2](https://doi.org/10.1175/1520-0485(1998)028<0433:GVOTFB>2.0.CO;2).
- 639 Chelton, D. B., M. G. Schlax, and R. M. Samelson, 2011: Global observations of nonlinear
640 mesoscale eddies. *Progress in Oceanography*, **91** (2), 167–216, [https://doi.org/10.1016/j.pocean.](https://doi.org/10.1016/j.pocean.2011.01.002)
641 [2011.01.002](https://doi.org/10.1016/j.pocean.2011.01.002).

- Chen, R., S. T. Gille, J. L. McClean, G. R. Flierl, and A. Griesel, 2015: A multiwavenumber theory for eddy diffusivities and its application to the Southeast Pacific (DIMES) Region. *Journal of Physical Oceanography*, **45** (7), 1877–1896, <https://doi.org/10.1175/JPO-D-14-0229.1>.
- Chen, R., J. L. McClean, S. T. Gille, and A. Griesel, 2014: Isopycnal Eddy Diffusivities and Critical Layers in the Kuroshio Extension from an Eddying Ocean Model. *Journal of Physical Oceanography*, **44** (8), 2191–2211, <https://doi.org/10.1175/JPO-D-13-0258.1>.
- Chouksey, A., A. Griesel, M. Chouksey, and C. Eden, 2022: Changes in Global Ocean Circulation due to Isopycnal Diffusion. *Journal of Physical Oceanography*, **52** (9), 2219–2235, <https://doi.org/10.1175/JPO-D-21-0205.1>.
- Csanady, G. T., 1976: Topographic Waves in Lake Ontario. *Journal of Physical Oceanography*, **6** (1), 93–103, [https://doi.org/10.1175/1520-0485\(1976\)006<0093:TWILO>2.0.CO;2](https://doi.org/10.1175/1520-0485(1976)006<0093:TWILO>2.0.CO;2).
- Davis, R. E., 1987: Modeling eddy transport of passive tracers. *Journal of Marine Research*, **45** (3), 635–666, <https://doi.org/10.1357/002224087788326803>.
- Davis, R. E., 1991: Observing the general circulation with floats. *Deep Sea Research Part A. Oceanographic Research Papers*, **38**, S531–S571, [https://doi.org/10.1016/S0198-0149\(12\)80023-9](https://doi.org/10.1016/S0198-0149(12)80023-9).
- DelSole, T., 2004: Stochastic models of quasigeostrophic turbulence. *Surveys in Geophysics*, **25** (2), 107–149, <https://doi.org/10.1023/B:GEOP.00000028164.58516.b2>.
- Dijkstra, H. A., 2008: *Dynamical Oceanography*. Springer US, <https://doi.org/10.1007/978-3-540-76376-5>.
- Dritschel, D. G., and M. E. McIntyre, 2008: Multiple Jets as PV Staircases: The Phillips Effect and the Resilience of Eddy-Transport Barriers. *Journal of the Atmospheric Sciences*, **65** (3), 855–874, <https://doi.org/10.1175/2007JAS2227.1>.
- Eady, E. T., 1949: Long Waves and Cyclone Waves. *Tellus*, **1** (3), 33–52, <https://doi.org/10.3402/tellusa.v1i3.8507>.
- Eden, C., 2007: Eddy length scales in the North Atlantic Ocean. *Journal of Geophysical Research*, **112** (C6), C06 004, <https://doi.org/10.1029/2006JC003901>.

- 669 Eden, C., 2011: A closure for meso-scale eddy fluxes based on linear instability theory. *Ocean*
670 *Modelling*, **39** (3-4), 362–369, <https://doi.org/10.1016/j.ocemod.2011.05.009>.
- 671 Eden, C., and R. J. Greatbatch, 2008: Towards a mesoscale eddy closure. *Ocean Modelling*, **20** (3),
672 223–239, <https://doi.org/10.1016/j.ocemod.2007.09.002>.
- 673 Ferrari, R., and M. Nikurashin, 2010: Suppression of eddy diffusivity across jets in the
674 Southern Ocean. *Journal of Physical Oceanography*, **40** (7), 1501–1519, [https://doi.org/](https://doi.org/10.1175/2010JPO4278.1)
675 10.1175/2010JPO4278.1.
- 676 Ferreira, D., J. Marshall, and P. Heimbach, 2005: Estimating Eddy Stresses by Fitting Dynamics
677 to Observations Using a Residual-Mean Ocean Circulation Model and Its Adjoint. *Journal of*
678 *Physical Oceanography*, **35** (10), 1891–1910, <https://doi.org/10.1175/JPO2785.1>.
- 679 Fox-Kemper, B., R. Ferrari, and R. Hallberg, 2008: Parameterization of Mixed Layer Eddies. Part
680 I: Theory and Diagnosis. *Journal of Physical Oceanography*, **38** (6), 1145–1165, [https://doi.org/](https://doi.org/10.1175/2007JPO3792.1)
681 10.1175/2007JPO3792.1.
- 682 Fox-Kemper, B., and Coauthors, 2019: Challenges and Prospects in Ocean Circulation Models.
683 *Frontiers in Marine Science*, **6**, 65, <https://doi.org/10.3389/fmars.2019.00065>.
- 684 Gent, P. R., and J. C. McWilliams, 1990: Isopycnal Mixing in Ocean Circulation Models. *Journal of*
685 *Physical Oceanography*, **20** (1), 150–155, [https://doi.org/10.1175/1520-0485\(1990\)020<0150:](https://doi.org/10.1175/1520-0485(1990)020<0150:IMIOCM>2.0.CO;2)
686 IMIOCM>2.0.CO;2.
- 687 Gent, P. R., J. Willebrand, T. J. McDougall, and J. C. McWilliams, 1995: Parameterizing Eddy-
688 Induced Tracer Transports in Ocean Circulation Models. *Journal of Physical Oceanography*,
689 **25** (4), 463–474, [https://doi.org/10.1175/1520-0485\(1995\)025<0463:PEITTI>2.0.CO;2](https://doi.org/10.1175/1520-0485(1995)025<0463:PEITTI>2.0.CO;2).
- 690 Gnanadesikan, A., D. Bianchi, and M.-A. Pradal, 2013: Critical role for mesoscale eddy diffusion
691 in supplying oxygen to hypoxic ocean waters. *Geophysical Research Letters*, **40** (19), 5194–5198,
692 <https://doi.org/10.1002/grl.50998>.
- 693 Gnanadesikan, A., M.-A. Pradal, and R. Abernathey, 2015: Isopycnal mixing by mesoscale
694 eddies significantly impacts oceanic anthropogenic carbon uptake. *Geophysical Research Letters*,
695 **42** (11), 4249–4255, <https://doi.org/10.1002/2015GL064100>.

- 696 Gnanadesikan, A., A. Russell, M.-A. Pradal, and R. Abernathey, 2017: Impact of Lateral Mixing
697 in the Ocean on El Nino in a Suite of Fully Coupled Climate Models. *Journal of Advances in*
698 *Modeling Earth Systems*, **9** (7), 2493–2513, <https://doi.org/10.1002/2017MS000917>.
- 699 Green, J. S. A., 1960: A problem in baroclinic stability. *Quarterly Journal of the Royal Meteorological Society*, **86** (368), 237–251, <https://doi.org/10.1002/qj.49708636813>.
- 701 Griesel, A., C. Eden, N. Koopmann, and E. Yulaeva, 2015: Comparing isopycnal eddy diffusiv-
702 ities in the Southern Ocean with predictions from linear theory. *Ocean Modelling*, **94**, 33–45,
703 <https://doi.org/10.1016/j.ocemod.2015.08.001>.
- 704 Griffies, S. M., 1998: The Gent–McWilliams Skew Flux. *Journal of Physical Oceanography*,
705 **28** (5), 831–841, [https://doi.org/10.1175/1520-0485\(1998\)028<0831:TGMSF>2.0.CO;2](https://doi.org/10.1175/1520-0485(1998)028<0831:TGMSF>2.0.CO;2).
- 706 Groeskamp, S., S. M. Griffies, D. Iudicone, R. Marsh, A. J. Nurser, and J. D. Zika, 2019: The
707 water mass transformation framework for ocean physics and biogeochemistry. *Annual Review of*
708 *Marine Science*, **11**, 271–305, <https://doi.org/10.1146/annurev-marine-010318-095421>.
- 709 Groeskamp, S., J. H. LaCasce, T. J. McDougall, and M. Rogé, 2020: Full-Depth Global Estimates of
710 Ocean Mesoscale Eddy Mixing From Observations and Theory. *Geophysical Research Letters*,
711 **47** (18), 1–12, <https://doi.org/10.1029/2020GL089425>.
- 712 Grooms, I., A. J. Majda, and K. S. Smith, 2015: Stochastic superparameterization in a
713 quasigeostrophic model of the Antarctic Circumpolar Current. *Ocean Modelling*, **85**, 1–15,
714 <https://doi.org/10.1016/j.ocemod.2014.10.001>.
- 715 Gruber, N., Z. Lachkar, H. Frenzel, P. Marchesiello, M. Münnich, J. C. McWilliams, T. Nagai,
716 and G.-K. Plattner, 2011: Eddy-induced reduction of biological production in eastern boundary
717 upwelling systems. *Nature Geoscience*, **4** (11), 787–792, <https://doi.org/10.1038/ngeo1273>.
- 718 Hallberg, R., 2013: Using a resolution function to regulate parameterizations of oceanic mesoscale
719 eddy effects. *Ocean Modelling*, **72**, 92–103, <https://doi.org/10.1016/j.ocemod.2013.08.007>.
- 720 Hogg, N. G., 2000: Low-frequency variability on the western flanks of the Grand Banks. *Journal*
721 *of Marine Research*, **58** (4), 523–545, <https://doi.org/10.1357/002224000321511007>.

- Holloway, G., 1986: Estimation of oceanic eddy transports from satellite altimetry. *Nature*, **323 (6085)**, 243–244, <https://doi.org/10.1038/323243a0>.
- Holloway, G., and S. S. Kristmannsson, 1984: Stirring and transport of tracer fields by geostrophic turbulence. *Journal of Fluid Mechanics*, **141**, 27–50.
- Holmes, R. M., S. Groeskamp, K. D. Stewart, and T. J. McDougall, 2022: Sensitivity of a Coarse-Resolution Global Ocean Model to a Spatially Variable Neutral Diffusivity. *Journal of Advances in Modeling Earth Systems*, **14 (3)**, <https://doi.org/10.1029/2021MS002914>.
- Isachsen, P. E., 2011: Baroclinic instability and eddy tracer transport across sloping bottom topography: How well does a modified Eady model do in primitive equation simulations? *Ocean Modelling*, **39 (1-2)**, 183–199, <https://doi.org/10.1016/j.ocemod.2010.09.007>.
- Isachsen, P. E., and O. A. Nøst, 2012: The air-sea transformation and residual overturning circulation within the Nordic Seas. *Journal of Marine Research*, **70 (1)**, 31–68, <https://doi.org/10.1357/002224012800502372>.
- Jansen, M. F., A. Adcroft, S. Khani, and H. Kong, 2019: Toward an Energetically Consistent, Resolution Aware Parameterization of Ocean Mesoscale Eddies. *Journal of Advances in Modeling Earth Systems*, **11 (8)**, 2844–2860, <https://doi.org/10.1029/2019MS001750>.
- Jansen, M. F., A. J. Adcroft, R. Hallberg, and I. M. Held, 2015: Parameterization of eddy fluxes based on a mesoscale energy budget. *Ocean Modelling*, **92**, 28–41, <https://doi.org/10.1016/j.ocemod.2015.05.007>.
- Jones, C. S., and R. P. Abernathey, 2019: Isopycnal Mixing Controls Deep Ocean Ventilation. *Geophysical Research Letters*, **46 (22)**, 13 144–13 151, <https://doi.org/10.1029/2019GL085208>.
- Juricke, S., S. Danilov, N. Koldunov, M. Oliver, D. V. Sein, D. Sidorenko, and Q. Wang, 2020a: A Kinematic Kinetic Energy Backscatter Parametrization: From Implementation to Global Ocean Simulations. *Journal of Advances in Modeling Earth Systems*, **12 (12)**, <https://doi.org/10.1029/2020MS002175>.
- Juricke, S., S. Danilov, N. Koldunov, M. Oliver, and D. Sidorenko, 2020b: Ocean Kinetic Energy Backscatter Parametrization on Unstructured Grids: Impact on Global Eddy-

749 Permitting Simulations. *Journal of Advances in Modeling Earth Systems*, **12** (1), [https://doi.org/](https://doi.org/10.1029/2019MS001855)
750 10.1029/2019MS001855.

751 Keffer, T., and G. Holloway, 1988: Estimating Southern Ocean eddy flux of heat and salt from
752 satellite altimetry. *Nature*, **332** (6165), 624–626, <https://doi.org/10.1038/332624a0>.

753 Khani, S., M. F. Jansen, and A. Adcroft, 2019: Diagnosing Subgrid Mesoscale Eddy Fluxes With
754 and Without Topography. *Journal of Advances in Modeling Earth Systems*, **11** (12), 3995–4015,
755 <https://doi.org/10.1029/2019MS001721>.

756 Kjellsson, J., and L. Zanna, 2017: The Impact of Horizontal Resolution on Energy Transfers in
757 Global Ocean Models. *Fluids*, **2** (3), 45, <https://doi.org/10.3390/fluids2030045>.

758 Klocker, A., and R. Abernathey, 2014: Global patterns of mesoscale eddy properties and dif-
759 fusivities. *Journal of Physical Oceanography*, **44** (3), 1030–1046, [https://doi.org/10.1175/](https://doi.org/10.1175/JPO-D-13-0159.1)
760 JPO-D-13-0159.1.

761 Klocker, A., R. Ferrari, and J. H. LaCasce, 2012: Estimating suppression of eddy mixing by
762 mean flows. *Journal of Physical Oceanography*, **42** (9), 1566–1576, [https://doi.org/10.1175/](https://doi.org/10.1175/JPO-D-11-0205.1)
763 JPO-D-11-0205.1.

764 Kong, H., and M. F. Jansen, 2017: The eddy diffusivity in barotropic β -plane turbulence. *Fluids*,
765 **2** (4), <https://doi.org/10.3390/fluids2040054>.

766 LaCasce, J., 2008: Statistics from Lagrangian observations. *Progress in Oceanography*, **77** (1),
767 1–29, <https://doi.org/10.1016/j.pocean.2008.02.002>.

768 LaCasce, J. H., 2000: Floats and f/H. *Journal of Marine Research*, **58**, 61–95, [https://doi.org/](https://doi.org/10.1357/002224000321511205)
769 10.1357/002224000321511205.

770 LaCasce, J. H., 2017: The Prevalence of Oceanic Surface Modes. *Geophysical Research Letters*,
771 **44** (21), <https://doi.org/10.1002/2017GL075430>.

772 LaCasce, J. H., R. Ferrari, J. Marshall, R. Tulloch, D. Balwada, and K. Speer, 2014: Float-Derived
773 Isopycnal Diffusivities in the DIMES Experiment. *Journal of Physical Oceanography*, **44** (2),
774 764–780, <https://doi.org/10.1175/JPO-D-13-0175.1>.

LaCasce, J. H., and S. Groeskamp, 2020: Baroclinic modes over rough bathymetry and the surface deformation radius. *Journal of Physical Oceanography*, **50** (10), 2835–2847, <https://doi.org/10.1175/JPO-D-20-0055.1>.

LaCasce, J. H., and K. G. Speer, 1999: Lagrangian statistics in unforced barotropic flows. *Journal of Marine Research*, **57**, 245–274.

Larichev, V., and I. Held, 1995: Eddy amplitudes and fluxes in a homogeneous model of fully developed baroclinic instability. *Journal of Physical Oceanography*, **25** (10), 2285–2297.

Ledwell, J. R., A. J. Watson, and C. S. Law, 1993: Evidence for slow mixing across the pycnocline from an open-ocean tracer-release experiment. *Nature*, **364** (6439), 701–703, <https://doi.org/10.1038/364701a0>.

Ledwell, J. R., A. J. Watson, and C. S. Law, 1998: Mixing of a tracer in the pycnocline. *Journal of Geophysical Research: Oceans*, **103** (C10), 21 499–21 529, <https://doi.org/10.1029/98JC01738>.

Lee, M.-M., A. J. G. Nurser, A. C. Coward, and B. A. de Cuevas, 2007: Eddy Advective and Diffusive Transports of Heat and Salt in the Southern Ocean. *Journal of Physical Oceanography*, **37** (5), 1376–1393, <https://doi.org/10.1175/JPO3057.1>.

Mak, J., A. Avdis, T. David, H. S. Lee, Y. Na, Y. Wang, and F. E. Yan, 2022a: On Constraining the Mesoscale Eddy Energy Dissipation Time-Scale. *Journal of Advances in Modeling Earth Systems*, **14** (11), e2022MS003 223, <https://doi.org/10.1029/2022MS003223>.

Mak, J., J. R. Maddison, D. P. Marshall, and D. R. Munday, 2018: Implementation of a Geometrically Informed and Energetically Constrained Mesoscale Eddy Parameterization in an Ocean Circulation Model. *Journal of Physical Oceanography*, **48** (10), 2363–2382, <https://doi.org/10.1175/JPO-D-18-0017.1>.

Mak, J., D. Marshall, J. Maddison, and S. Bachman, 2017: Emergent eddy saturation from an energy constrained eddy parameterisation. *Ocean Modelling*, **112**, 125–138, <https://doi.org/10.1016/j.ocemod.2017.02.007>.

Mak, J., D. P. Marshall, G. Madec, and J. R. Maddison, 2022b: Acute Sensitivity of Global Ocean Circulation and Heat Content to Eddy Energy Dissipation Timescale. *Geophysical Research Letters*, **49** (8), e2021GL097 259, <https://doi.org/10.1029/2021GL097259>.

- 803 Marshall, J., E. Shuckburgh, H. Jones, and C. Hill, 2006: Estimates and Implications of Surface
804 Eddy Diffusivity in the Southern Ocean Derived from Tracer Transport. *Journal of Physical*
805 *Oceanography*, **36**, 1806–1821.
- 806 Martínez-Moreno, J., A. M. Hogg, and M. H. England, 2022: Climatology, Seasonality, and
807 Trends of Spatially Coherent Ocean Eddies. *Journal of Geophysical Research: Oceans*, **127** (7),
808 <https://doi.org/10.1029/2021JC017453>.
- 809 McDougall, T. J., and P. C. McIntosh, 2001: The Temporal-Residual-Mean Velocity. Part II: Isopy-
810 cnal Interpretation and the Tracer and Momentum Equations. *Journal of Physical Oceanography*,
811 **31** (5), 1222–1246, [https://doi.org/10.1175/1520-0485\(2001\)031<1222:TTRMVP>2.0.CO;2](https://doi.org/10.1175/1520-0485(2001)031<1222:TTRMVP>2.0.CO;2).
- 812 Meredith, M. P., A. C. Naveira Garabato, A. M. Hogg, and R. Farneti, 2012: Sensitivity of the
813 Overturning Circulation in the Southern Ocean to Decadal Changes in Wind Forcing. *Journal*
814 *of Climate*, **25** (1), 99–110, <https://doi.org/10.1175/2011JCLI4204.1>.
- 815 Nakamura, N., and D. Zhu, 2010a: Finite-Amplitude Wave Activity and Diffusive Flux of Potential
816 Vorticity in Eddy–Mean Flow Interaction. *Journal of the Atmospheric Sciences*, **67** (9), 2701–
817 2716, <https://doi.org/10.1175/2010JAS3432.1>.
- 818 Nakamura, N., and D. Zhu, 2010b: Formation of Jets through Mixing and Forcing of Potential
819 Vorticity: Analysis and Parameterization of Beta-Plane Turbulence. *Journal of the Atmospheric*
820 *Sciences*, **67** (9), 2717–2733, <https://doi.org/10.1175/2009JAS3159.1>.
- 821 Naveira Garabato, A. C., R. Ferrari, and K. L. Polzin, 2011: Eddy stirring in the Southern Ocean.
822 *Journal of Geophysical Research: Oceans*, **116** (9), <https://doi.org/10.1029/2010JC006818>.
- 823 Nummelin, A., 2023a: Parameterizing mesoscale eddy buoyancy transport over sloping topog-
824 raphy – data. [Dataset]. NIRD research data archive, URL [dx.doi.org/10.11582/2023.00129](https://doi.org/10.11582/2023.00129),
825 <https://doi.org/10.11582/2023.00129>.
- 826 Nummelin, A., 2023b: Parameterizing mesoscale eddy buoyancy transport over sloping topography
827 – model setup. [Software]. Zenodo, URL [dx.doi.org/10.5281/zenodo.8227382](https://doi.org/10.5281/zenodo.8227382), <https://doi.org/10.5281/zenodo.8227382>.
828

- 829 Nummelin, A., and P. E. Isachsen, 2024: Parameterizing mesoscale eddy buoyancy transport
830 over sloping topography. Preprint, accepted for publication in J. Adv. Model. Earth Syst.
831 <https://doi.org/10.22541/essoar.168394750.04852652/v2>.
- 832 Pedlosky, J., 1987: *Geophysical Fluid Dynamics*. Springer, New York.
- 833 Pennel, R., and I. Kamenkovich, 2014: On the Factors Controlling the Eddy-Induced Transport
834 in the Antarctic Circumpolar Current. *Journal of Physical Oceanography*, **44** (8), 2127–2138,
835 <https://doi.org/10.1175/JPO-D-13-0256.1>.
- 836 Pradal, M.-A., and A. Gnanadesikan, 2014: How does the Redi parameter for mesoscale mixing
837 impact global climate in an Earth System Model? *Journal of Advances in Modeling Earth*
838 *Systems*, **6** (3), 586–601, <https://doi.org/10.1002/2013MS000273>.
- 839 Prandtl, L., 1925: Bericht über Untersuchungen zur ausgebildeten Turbulenz. *Zeitschrift für Ange-*
840 *wandte Mathematik und Mechanik*, **5**, 136–139.
- 841 Pringle, J. M., 2001: Cross-shelf eddy heat transport in a wind-free coastal ocean undergoing winter
842 time cooling. *Journal of Geophysical Research: Oceans*, **106** (C2), 2589–2604, <https://doi.org/10.1029/2000JC900148>.
- 844 Redi, M. H., 1982: Oceanic Isopycnal Mixing by Coordinate Rotation. *Journal of Physi-*
845 *cal Oceanography*, **12** (10), 1154–1158, [https://doi.org/10.1175/1520-0485\(1982\)012<1154:OIMBCR>2.0.CO;2](https://doi.org/10.1175/1520-0485(1982)012<1154:OIMBCR>2.0.CO;2).
- 847 Rhines, P., 1970: Edge-, bottom-, and Rossby waves in a rotating stratified fluid. *Geophysical and*
848 *Astrophysical Fluid Dynamics*, **1** (3-4), 273–302, <https://doi.org/10.1080/03091927009365776>.
- 849 Roach, C. J., D. Balwada, and K. Speer, 2016: Horizontal mixing in the Southern Ocean from Argo
850 float trajectories. *Journal of Geophysical Research: Oceans*, **121** (8), 5570–5586, <https://doi.org/10.1002/2015JC011440>.
- 852 Roach, C. J., D. Balwada, and K. Speer, 2018: Global Observations of Horizontal Mixing from
853 Argo Float and Surface Drifter Trajectories. *Journal of Geophysical Research: Oceans*, **123** (7),
854 4560–4575, <https://doi.org/10.1029/2018JC013750>.

- 855 Sallée, J., K. Speer, and S. Rintoul, 2011: Mean-flow and topographic control on surface eddy-
856 mixing in the Southern Ocean. *Journal of Marine Research*, **69** (4), 753–777, [https://doi.org/](https://doi.org/10.1357/002224011799849408)
857 10.1357/002224011799849408.
- 858 Seland, Ø., and Coauthors, 2020: Overview of the Norwegian Earth System Model (NorESM2)
859 and key climate response of CMIP6 DECK, historical, and scenario simulations. *Geoscientific*
860 *Model Development*, **13** (12), 6165–6200, <https://doi.org/10.5194/gmd-13-6165-2020>.
- 861 Srinivasan, K., and W. R. Young, 2014: Reynolds stress and eddy diffusivity of ss-plane
862 shear flow. *Journal of the Atmospheric Sciences*, **71** (6), 2169–2185, [https://doi.org/10.1175/](https://doi.org/10.1175/JAS-D-13-0246.1)
863 JAS-D-13-0246.1.
- 864 Stammer, D., 1998: On Eddy Characteristics, Eddy Transports, and Mean Flow Properties.
865 *Journal of Physical Oceanography*, **28** (4), 727–739, [https://doi.org/10.1175/1520-0485\(1998\)](https://doi.org/10.1175/1520-0485(1998)028<0727:OECETA>2.0.CO;2)
866 028<0727:OECETA>2.0.CO;2.
- 867 Stewart, A. L., A. Klocker, and D. Menemenlis, 2018: Circum-Antarctic Shoreward Heat Transport
868 Derived From an Eddy- and Tide-Resolving Simulation. *Geophysical Research Letters*, **45** (2),
869 834–845, <https://doi.org/10.1002/2017GL075677>.
- 870 Stewart, A. L., and A. F. Thompson, 2016: Eddy Generation and Jet Formation via Dense Water
871 Outflows across the Antarctic Continental Slope. *Journal of Physical Oceanography*, **46** (12),
872 3729–3750, <https://doi.org/10.1175/JPO-D-16-0145.1>.
- 873 Stewart, K. D., P. Spence, S. Waterman, J. Le Sommer, J.-M. Molines, J. M. Lilly, and M. H.
874 England, 2015: Anisotropy of eddy variability in the global ocean. *Ocean Modelling*, **95**,
875 53–65, <https://doi.org/10.1016/j.ocemod.2015.09.005>.
- 876 Straub, D. N., 1994: Dispersive effects of zonally varying topography on quasigeostrophic Rossby
877 waves. *Geophysical and Astrophysical Fluid Dynamics*, **75** (2-4), 107–130, [https://doi.org/](https://doi.org/10.1080/03091929408203650)
878 10.1080/03091929408203650.
- 879 Taylor, G. I., 1921: Diffusion by Continuous Movements. *Proceedings of the London Mathematical*
880 *Society*, **20**, 196–211.

881 Thompson, A. F., 2010: Jet Formation and Evolution in Baroclinic Turbulence with Simple
 882 Topography. *Journal of Physical Oceanography*, **40** (2), 257–278, [https://doi.org/10.1175/](https://doi.org/10.1175/2009JPO4218.1)
 883 2009JPO4218.1.

884 Tulloch, R., and Coauthors, 2014: Direct Estimate of Lateral Eddy Diffusivity Upstream of
 885 Drake Passage. *Journal of Physical Oceanography*, **44** (10), 2593–2616, [https://doi.org/10.](https://doi.org/10.1175/JPO-D-13-0120.1)
 886 1175/JPO-D-13-0120.1.

887 Vallis, G. K., and M. E. Maltrud, 1993: Generation of Mean Flows and Jets on a Beta Plane and
 888 over Topography. *Journal of Physical Oceanography*, **23**, 1346–1362.

889 Wang, Y., and A. L. Stewart, 2020: Scalings for eddy buoyancy transfer across continental slopes
 890 under retrograde winds. *Ocean Modelling*, **147**, 101 579, [https://doi.org/10.1016/j.ocemod.2020.](https://doi.org/10.1016/j.ocemod.2020.101579)
 891 101579.

892 Wei, H., and Y. Wang, 2021: Full-Depth Scalings for Isopycnal Eddy Mixing Across Continental
 893 Slopes Under Upwelling-Favorable Winds. *Journal of Advances in Modeling Earth Systems*,
 894 **13** (6), 1–40, <https://doi.org/10.1029/2021MS002498>.

895 Wei, H., Y. Wang, and J. Mak, 2024: Parameterizing Eddy Buoyancy Fluxes Across Prograde
 896 Shelf/Slope Fronts Using a Slope-Aware GEOMETRIC Closure. *Journal of Physical Oceanog-*
 897 *raphy*, **54** (2), 359–377, <https://doi.org/10.1175/JPO-D-23-0152.1>.

898 Wei, H., Y. Wang, A. L. Stewart, and J. Mak, 2022: Scalings for Eddy Buoyancy Fluxes
 899 Across Prograde Shelf/Slope Fronts. *Journal of Advances in Modeling Earth Systems*, **14** (12),
 900 <https://doi.org/10.1029/2022MS003229>.

901 Wolfram, P. J., and T. D. Ringler, 2017: Quantifying Residual, Eddy, and Mean Flow Effects
 902 on Mixing in an Idealized Circumpolar Current. *Journal of Physical Oceanography*, **47** (8),
 903 1897–1920, <https://doi.org/10.1175/JPO-D-16-0101.1>.

904 Wortham, C., and C. Wunsch, 2014: A multidimensional spectral description of ocean variability.
 905 *Journal of Physical Oceanography*, **44** (3), 944–966, <https://doi.org/10.1175/JPO-D-13-0113.1>.

906 Wunsch, C., 2010: Toward a midlatitude ocean frequency-wavenumber spectral density and trend
 907 determination. *Journal of Physical Oceanography*, **40** (10), 2264–2281, [https://doi.org/10.1175/](https://doi.org/10.1175/2010JPO4376.1)
 908 2010JPO4376.1.

- 909 Xie, J., H. Liu, and P. Lin, 2023: A Multifaceted Isonutral Eddy Transport Diagnostic Framework
910 and Its Application in the Southern Ocean. *Journal of Advances in Modeling Earth Systems*,
911 **15** (7), e2023MS003728, <https://doi.org/10.1029/2023MS003728>.
- 912 Yankovsky, E., L. Zanna, and K. S. Smith, 2022: Influences of Mesoscale Ocean Eddies on Flow
913 Vertical Structure in a Resolution-Based Model Hierarchy. *Journal of Advances in Modeling
914 Earth Systems*, **14** (11), <https://doi.org/10.1029/2022MS003203>.
- 915 Zanna, L., P. Porta Mana, J. Anstey, T. David, and T. Bolton, 2017: Scale-aware deterministic
916 and stochastic parametrizations of eddy-mean flow interaction. *Ocean Modelling*, **111**, 66–80,
917 <https://doi.org/10.1016/j.ocemod.2017.01.004>.
- 918 Zika, J. D., J.-B. Sallée, A. J. S. Meijers, A. C. Naveira-Garabato, A. J. Watson, M.-J. Messias,
919 and B. A. King, 2020: Tracking the spread of a passive tracer through Southern Ocean water
920 masses. *Ocean Science*, **16** (2), 323–336, <https://doi.org/10.5194/os-16-323-2020>.